Binary neutron star mergers in massive scalar-tensor theory: Properties of postmerger remnants

Alan Tsz-Lok Lam[1,*] Hao-Jui Kuan,[1] Masaru Shibata,[1,2] Karim Van Aelst,[1] and Kenta Kiuchi[1,2]

[1]*Max Planck Institute for Gravitational Physics (Albert Einstein Institute), 14476 Potsdam, Germany*
[2]*Center of Gravitational Physics and Quantum Information, Yukawa Institute for Theoretical Physics, Kyoto University, Kyoto 606-8502, Japan*

We investigate the properties of postmerger remnants of binary neutron star mergers in the framework of Damour–Esposito-Farese-type scalar-tensor theory of gravity with a massive scalar field by numerical relativity simulation. It is found that the threshold mass for prompt collapse is raised in the presence of the excited scalar field. Our simulation results also suggest the existence of a long-lived ϕ mode in hypermassive neutron stars due to the presence of the massive scalar field that enhances the quasiradial oscillation in the remnant. We investigate the descalarization condition in hypermassive neutron stars and discover a distinctive signature in postmerger gravitational waves.

I. INTRODUCTION

After the monumental event GW170817 [1–4], huge effort has been devoted to modeling the physics involved in the course of binary neutron star (BNS) mergers with the hope of learning more about the nuclear equation of state (EOS) of matters in extreme environment, exploring r-process nucleosynthesis in the merger ejecta, and understanding the nonlinear nature of gravity. In particular, through measuring the size of matter effects of the neutron star (NS) members in the late inspiral stages for this event, the stiffness of the EOS has been constrained to a narrow range [5–9]. In addition, general relativity (GR) has proven to accurately reproduce gravitational effects at least up to the stage shortly before the merger. Considering the Damour–Esposito-Farese type extension to GR (DEF theory in what follows), this can be translated to an upper bound on the coupling constant, which prohibits spontaneous scalarization in isolated NSs for massless scalar fields [10] while admitting mild scalarization for massive cases [11]. A plausible agent to push the known constraints further is the remnant system in the aftermath of the merger, where higher-energy physics, for which details have not been yet understood, can play an important role. The evolution process of BNS remnants is also the key

determinant of multimessenger signals [12,13]: the properties of the electromagnetic (EM) signals depend strongly on the mass and the composition of ejecta from the remnant, including some ultrarelativistic jets [14], and postmerger gravitational waves (GWs) encode information about BNS parameters [15–17].

Joint detection of EM and GW signals provides a unique avenue to learn the details of postmerger systems such as the lifetime of the remnant NSs. The latter quantity is sensitive to the EOS and underlying gravitational theory. Although GR functions quite well throughout the inspiral history of binaries, beyond-GR signatures may reveal shortly before, during, and after the merger. For example, the DEF theory can admit dynamical scalarization and/or an enhanced scalar cloud in the parameter region corresponding to GW170817 [11]. Additionally, the additional scalar degree of freedom can lead to qualitative differences in the postmerger waveform and impact the evolution of the object produced in the merger. The goal here is thus to extensively investigate the outcomes of BNS mergers in the DEF theory, whereas magnetic, neutrino, and thermal physics are not taken into account, as we focus on the postmerger stage only for a short timescale.

In most BNS mergers, either a hypermassive neutron star (HMNS, which is stabilized by a high degree of angular momentum with a differential rotation [18–20]) is formed and lives for some time before collapsing to a black hole, or a prompt collapse occurs if the total mass of the BNS exceeds a threshold M_{thr}. The threshold mass for the prompt collapse is sensitive to the nuclear EOS [12,21]. On the other hand, it is expected to be rare that a supramassive NS is produced from a BNS since the total mass of the system should be less than the maximum mass that is

---

supportable by rigid rotation (M_c). An empirical relation of such critical value is $M_c \simeq 1.2 M_{\text{TOV}}$, where M_{TOV} is the maximum mass of a spherical cold NS of a given EOS [22–24], which then suggests $M_c \lesssim 2.6 M_\odot$ (e.g., [25,26]). Some population studies thus suggest that only $\lesssim 15\%$ of BNSs have a total mass lower than M_c [27] (see also [28]). In the present work, we focus on scenarios with total mass larger than M_c, i.e., a black hole + torus will be formed either shortly after the merger or after the rotational profile is modified within the HMNS [29,30].

The presence of a torus surrounding the black hole plays an essential role in determining the postmerger emissions, such as short γ ray bursts [21,31] and kilonovae [32–35]. The amount of matter ejected to form the torus depends strongly on the total mass and the nuclear EOS for both prompt collapse and HMNS formation scenarios [16,36–38] (see also [12] for a review). In the latter scenario, the lifetime of HMNS τ_{H} is the main factor that determines the torus mass, especially when the BNS is of (nearly) equal mass, since the matter injection from the central object ceases upon the formation of the black hole [30].

It has been known that the value of τ_{H} for short-lived HMNSs is determined primarily by the BNS's total mass if the system is moderately symmetric (e.g., [13,21,36,39–41]) in GR. Under the framework of the DEF theory, the lifetime of HMNSs is also likely to be sensitive to the scalar parameters, which are the strength of the coupling (B) of the scalar field to the metric functions and the mass of the scalar field (m_ϕ). In addition to their lifetime, the scalar field can also exist in the HMNSs for a certain time, $\tau_{\text{S}}(\leq \tau_{\text{H}})$. Depending on τ_{H}, three possibilities for the outcome are generically expected: (i) prompt collapse to a black hole, (ii) short-lived HMNS formation, and (iii) long- but finite-lived HMNS formation. In the presence of an excited scalar field in the DEF theory, τ_{S} further divides channel (iii) into (iii.a) long-lived scalarized HMNSs and (iii.b) those descalarizing at some point. The two characteristic timescales are dependent on the source and theory parameters, namely, the total mass and mass ratio of the BNSs, (M_{tot}, q), the EOS, B, and m_ϕ. The main goal of the present study is to investigate how the two crucial timescales are modified by the scalar quantities by performing numerical relativity simulations for equal-mass BNSs.

The paper is organized as follows. Section II briefly introduces the DEF theory, the associated $3 + 1$ decomposition for numerical evolution, EOS employed, details of the numerical setup, and parameters we consider in this work. In Sec. III we discuss in detail the postmerger scenarios, including the formation of a long-lived HMNS, a short-lived HMNS, and prompt collapse to a black hole, and investigate the effect of the scalar field on the HMNS lifetime and the threshold mass. The properties of the remnant including dynamical ejecta, GW signal, and mass of the final black hole and disk with potential quantities relevant to observation are given in Sec. IV. Section V is devoted to summary and discussion. Throughout this paper, we employ the geometrical units $c = G_* = \hbar = 1$, where c, G_*, and $\hbar$ are the speed of light, the "bare" gravitational constant, and the reduced Planck constant, respectively. In the DEF theory, the gravitational constant in the action is $G = G_* \phi$. Subscripts $a, b, c, \ldots$ running from 0 to 3 denote the spacetime components, while $i, j, k, \ldots$ running from 1 to 3 denote the spatial components.

II. FORMALISM

In the so-called Jordan frame, the action of the DEF theory reads [42]

$$S = \frac{1}{16\pi} \int d^4x \sqrt{-g} \left[\phi \mathcal{R} - \frac{\omega(\phi)}{\phi} \nabla_a \phi \nabla^a \phi - U(\phi) \right] - S_{\text{matter}}, \tag{1}$$

where $\mathcal{R}$ is the Ricci scalar associated with metric g_{ab}, ϕ is the scalar field, S_{matter} is the action for matter, and $\omega(\phi)$ is chosen to have the form [43,44]

$$\frac{1}{\omega(\phi) + 3/2} = B \ln \phi, \tag{2}$$

for a coupling constant B. For the latter use, we introduce the auxiliary variable φ,

$$2 \ln \phi = \varphi^2, \tag{3}$$

with respect to which the scalar potential is defined as [11,45]

$$U(\phi) = \frac{2 m_\phi^2 \varphi^2 \phi^2}{B}, \tag{4}$$

where it can be seen that m_ϕ is the scalar mass when one rewrites the potential into the so-called Einstein frame. We assume that the asymptotic value of the scalar field φ_0 vanishes at the spacial infinity, the same as [11,45].

A. Evolutionary equations

The associated equations for the metric and scalar fields can be derived as (e.g., [11])

$$G_{ab} = 8\pi \phi^{-1} T_{ab} + \omega(\phi)\phi^{-2} \left[(\nabla_a \phi)(\nabla_b \phi) - \frac{1}{2} g_{ab} \nabla_c \phi \nabla^c \phi \right] + \phi^{-1} (\nabla_a \nabla_b \phi - g_{ab} \Box_g \phi) - \frac{m_\phi^2 \varphi^2 \phi}{B} g_{ab}, \tag{5a}$$

and

$$\nabla_a \nabla^a \phi = \frac{1}{2\omega(\phi) + 3}\left[8\pi T - \frac{d\omega}{d\phi}(\nabla_c\phi)(\nabla^c\phi) + \frac{4m_\phi^2\phi^2}{B}\right]$$
$$= 2\pi\varphi^2 BT + \phi^{-1}\varphi^{-2}(\nabla_c\phi)(\nabla^c\phi) + m_\phi^2\varphi^2\phi^2,$$
$$\tag{5b}$$

where G_{ab} and ∇_a are the Einstein tensor and covariant derivative associated with g_{ab}, and T_{ab} is the stress-energy tensor with $T := T_a{}^a$. Since we evolve φ rather than ϕ, we rewrite Eq. (5b) in terms of φ as

$$\nabla_a\nabla^a\varphi = 2\pi\phi^{-1}BT\varphi - \varphi(\nabla_c\varphi)(\nabla^c\varphi) + m_\phi^2\varphi\phi, \quad (6)$$

which will be used to derive the evolution equation for the auxiliary scalar field.

The evolution equations for gravitational and scalar fields can be derived by $3 + 1$ decomposition (see Ref. [43] for the detailed derivation in the massless DEF case). Following the Baumgarte-Shapiro-Shibata-Nakamura formalism [46,47], we can obtain the modified evolution equations in the Cartesian coordinates as follows [45]:

$$(\partial_t - \beta^k\partial_k)W = \frac{1}{3}W(\alpha K - \partial_k\beta^k), \tag{7}$$

$$(\partial_t - \beta^k\partial_k)\tilde{\gamma}_{ij} = -2\alpha\tilde{A}_{ij} + \tilde{\gamma}_{ik}\partial_j\beta^k + \tilde{\gamma}_{jk}\partial_i\beta^k - \frac{2}{3}\tilde{\gamma}_{ij}\partial_k\beta^k, \tag{8}$$

$$(\partial_t - \beta^k\partial_k)\tilde{A}_{ij} = W^2[\alpha R_{ij} - D_iD_j\alpha - 8\pi\alpha\phi^{-1}S_{ij}]^{\mathrm{TF}}$$
$$+ \alpha\left(K\tilde{A}_{ij} - 2\tilde{A}_{ik}\tilde{A}_j{}^k\right) + \tilde{A}_{kj}\partial_i\beta^k$$
$$+ \tilde{A}_{ki}\partial_j\beta^k - \frac{2}{3}\tilde{A}_{ij}\partial_k\beta^k + \alpha\tilde{A}_{ij}\varphi\Phi$$
$$- \alpha W^2[\omega\varphi^2 D_i\varphi D_j\varphi + \phi^{-1}D_iD_j\phi]^{\mathrm{TF}}, \tag{9}$$

$$(\partial_t - \beta^k\partial_k)K = 4\pi\alpha\phi^{-1}(S^i{}_i + \rho_{\mathrm{h}}) + \alpha K_{ij}K^{ij} - D_iD^i\alpha$$
$$+ \alpha\omega\varphi^2\Phi^2 - \left(\frac{3}{2} + \frac{1}{B}\right)\alpha m_\phi^2\varphi^2\phi$$
$$+ \alpha\phi^{-1}\left[D_iD^i\phi - K\Phi\phi\varphi - 3\pi\varphi^2 BT\right.$$
$$\left.+ \frac{3}{2\varphi^2\phi}\left(\Phi^2\phi^2\varphi^2 - D_k\phi D^k\phi\right)\right], \tag{10}$$

$$(\partial_t - \beta^k\partial_k)\tilde{\Gamma}^i = 2\alpha\left(\tilde{\Gamma}^i{}_{jk}\tilde{A}^{jk} - \frac{2}{3}\tilde{\gamma}^{ij}\partial_j K - \frac{3}{W}\tilde{A}^{ij}\partial_j W\right)$$
$$- 2\tilde{A}^{ij}\partial_j\alpha - 2\alpha\tilde{\gamma}^{ij}\left[8\pi\phi^{-1}J_j - \varphi K_j{}^k D_k\varphi\right.$$
$$\left.+ \left(1 + \frac{2}{B} - \frac{\varphi^2}{2}\right)\Phi D_j\varphi + \varphi D_j\Phi\right]$$
$$+ \tilde{\gamma}^{jk}\partial_j\partial_k\beta^i + \frac{1}{3}\tilde{\gamma}^{ij}\partial_j\partial_k\beta^k$$
$$- \tilde{\gamma}^{kl}\tilde{\Gamma}^j{}_{kl}\partial_j\beta^i + \frac{2}{3}\tilde{\gamma}^{jk}\tilde{\Gamma}^i{}_{jk}\partial_l\beta^l, \tag{11}$$

$$(\partial_t - \beta^k\partial_k)\varphi = -\alpha\Phi, \tag{12}$$

$$(\partial_t - \beta^k\partial_k)\Phi = -\alpha D_iD^i\varphi - (D_i\alpha)D^i\varphi - \alpha\varphi(\nabla_a\varphi)\nabla^a\varphi$$
$$+ \alpha K\Phi + 2\pi\alpha\phi^{-1}BT\varphi + \alpha m_\phi^2\varphi\phi, \tag{13}$$

where α is the lapse function, β^i is the shift vector, $\Phi := -n^a\nabla_a\varphi$ is the "momentum" of the scalar field with $n^a = (1/\alpha, -\beta^i/\alpha)$, γ_{ij} is the spatial metric with $\gamma := \det(\gamma_{ij})$, $W := \gamma^{-1/6}$, $\tilde{\gamma}_{ij} := \gamma^{-1/3}\gamma_{ij}$ is the conformal spatial metric, $\tilde{\Gamma}^i{}_{jk}$ is the Christoffel symbol of $\tilde{\gamma}_{ij}$ with $\tilde{\Gamma}^i := -\partial_j\tilde{\gamma}^{ij}$, $(S_{ij})^{\mathrm{TF}} := S_{ij} - \gamma_{ij}S^k{}_k/3$ denotes the trace-free part of the stress tensor S_{ij}, K_{ij} is the extrinsic curvature with $K := K^i{}_i$ being its trace, $\tilde{A}_{ij} := W^2(K_{ij})^{\mathrm{TF}}$ is the conformal traceless part of K_{ij}, $S_{ij} := \gamma^a{}_i\gamma^b{}_j T_{ab}$, $\rho_h := n^a n^b T_{ab}$, $J_i := -\gamma^a{}_i n^b T_{ab}$ are the spacetime decomposition of the stress-energy tensor, R_{ij} is the spatial Ricci tensor, and D_i is the covariant derivative with respect to the spatial metric. We adopt the moving-puncture gauge [48,49] for the lapse function and shift vector in the form

$$(\partial_t - \beta^j\partial_j)\alpha = -2\alpha K, \tag{14}$$

$$(\partial_t - \beta^j\partial_j)\beta^i = (3/4)B^i, \tag{15}$$

$$(\partial_t - \beta^j\partial_j)B^i = (\partial_t - \beta^j\partial_j)\tilde{\Gamma}^i - \eta_B B^i, \tag{16}$$

where B^i is an auxiliary variable and η_B is a parameter typically set to be $\sim 1/M_{\mathrm{tot}}$. The Hamiltonian and momentum constraints can be found in Eqs. (15) and (16) of [11], and will not be repeated here.

In the Jordan frame, the scalar field does not affect the matter evolution explicitly, and thus, the equations of motion for matter are the same as those in GR. We assume a perfect fluid [i.e., $S_{\mathrm{matter}} = \int d^4x\sqrt{-g}\rho(1 + \epsilon)$], for which the stress-energy tensor is expressed as

$$T^{ab} = \rho h u^a u^b + P g^{ab}, \tag{17}$$

and the conservation equations are given by

$$\nabla_a T^a{}_b = 0. \tag{18}$$

Here ρ is the rest-mass density, P is the pressure, ϵ is the specific internal energy, $h := 1 + \epsilon + P/\rho$ is the specific enthalpy, and u^a is the four-velocity of the fluid. In addition to Eq. (18), we solve the continuity equation, $\nabla_a(\rho u^a) = 0$.

B. Equation of state

We adopt the piecewise-polytropic approximation [50] for the barotropic EOS APR4 [51], MPA1 [52], and H4 [53], which cover a range of stiffness favored by GW170817 [5,9,54]. In addition, we adopt the following description for the thermal pressure, which is associated with the generation of shocks in the plunge and postmerger stages:

$$P = P_{\mathrm{cold}}(\rho) + P_{\mathrm{th}}(\rho, \epsilon), \tag{19}$$

where the cold contribution to the pressure $P_{\mathrm{cold}}(\rho)$ is dictated by the cold EOS, and the thermal contribution is assumed to take the form [55]

$$P_{\mathrm{th}} = (\Gamma_{\mathrm{th}} - 1)\rho\epsilon_{\mathrm{th}}, \tag{20}$$

with the adiabatic index Γ_{th} for heated matter, and $\epsilon_{\mathrm{th}} = \epsilon - \epsilon_{\mathrm{cold}}$ is the residual in the specific internal energy that is not included in the cold EOS. In general, Γ_{th} depends on the temperature and rest-mass density [56], while it has been suggested that a (reasonable) constant approximation suffices for investigating the fate of the merger remnant [36,39,57]. We choose $\Gamma_{\mathrm{th}} = 1.8$ for our simulations. Depending on the EOS and theory parameters, NSs in a coalescing BNS can remain unscalarized up to merger, be dynamically scalarized in the late inspiral, or be spontaneously scalarized at large separation [43,44,58–60].

C. Numerical setup

We implement the Z4c version of the evolution equations by extending the code developed in [61], which was parallelized to SACRA-MPI in [62]. SACRA-MPI employs a box-in-box adaptive mesh refinement with 2:1 refinement and imposes equatorial mirror symmetry on the $z = 0$ orbital plane. For the simulations shown in this article, each NS is covered by four comoving finer concentric boxes, with six coarser domains underneath containing both piles of the finer domains. The size of the finest domain is chosen to be about 1.3–1.5 times the NS radius. All domains are covered by $(2N, 2N, N)$ grid points for (x, y, z) with N being an even number. We employ the finite-volume scheme with a reflux prescription and Harten-Lax–Van Leer contact Riemann solver, as that implemented in [63], for hydrodynamics evolution to better conserve the total baryon mass of the system.

For the outer boundary condition, we use the outgoing boundary condition for metric variables following [46] and specifically include an additional term for the scalar-field variables $Q = (\varphi, \Phi)$ as

$$Q(t, r) = \left(1 - \frac{\Delta r}{r}\right)Q(t - \Delta t, r - \Delta r)e^{-m_\phi \Delta r}, \tag{21}$$

to capture the exponential decay tail due to the mass term m_ϕ. Here, $\Delta r = c\Delta t$ with Δt as the time step in numerical computation. We test the convergence of our code in three different resolutions (see Appendix A). Unless otherwise specified, we adopt $N = 94$ as the standard resolution of this paper, which corresponds to $\Delta x = 157$ m in the finest box. The details of the numerical setup can be found in Table I in Appendix A.

The primary purpose of this paper is to investigate how the scenarios of postmerger remnants depend on the binary mass, B, m_ϕ, and the EOS while restricting ourselves to equal-mass binaries. However, rather than specifying the binary mass as the sum of the Arnowitt-Deser-Misner (ADM) masses of the two NS members, we identify the binary mass as the total "rest mass,"

$$M_b := \int \rho u^t \sqrt{-g} d^3x, \tag{22}$$

contained in the binary. Taking into account the GW event GW170817, scalar masses of $m_\phi \gtrsim 10^{-11}$ eV are favored unless the coupling constant B is so small that the NSs in the observed system are nonscalarized [11]. This condition on m_ϕ is several orders of magnitude greater than the constraint concluded from the pulsar timing observations, which is $m_\phi \gtrsim 10^{-15}$ eV [64–66], while more rigorous Bayesian inference studies are required to transform the suggestion of $m_\phi \gtrsim 10^{-11}$ eV into a constraint (for strong couplings). On the other hand, a mass of $m_\phi \gtrsim 2 \times 10^{-11}$ eV would significantly suppress scalarization in NSs since the associated Compton length is shorter than the stellar size. Aiming to study the scalar's influence on BNS mergers, we focus on cases where NSs can develop a scalar cloud before and/or after merger, and thus the range of interest of m_ϕ is narrow. We will consider only one canonical value for the scalar mass, viz. $m_\phi = 1.33 \times 10^{-11}$ eV ($\lambdabar_{\mathrm{comp}} = 14.8$ km), to quantitatively study how B influences the lifetimes of the HMNSs (τ_{H}) and scalar cloud (τ_{S}) in postmerger systems.

For each EOS, we choose three different coupling strengths B such that an isolated NS with $M_b = 1.60 M_\odot$ would be either nonscalarized, marginally scalarized, or spontaneously scalarized as illustrated in Fig. 1. We explore a wide range of NS baryon masses spanning from $1.60 M_\odot$ to $1.90 M_\odot$ as summarized in Appendix B with Tables III–V for APR4, MPA1, and H4 EOS, respectively,
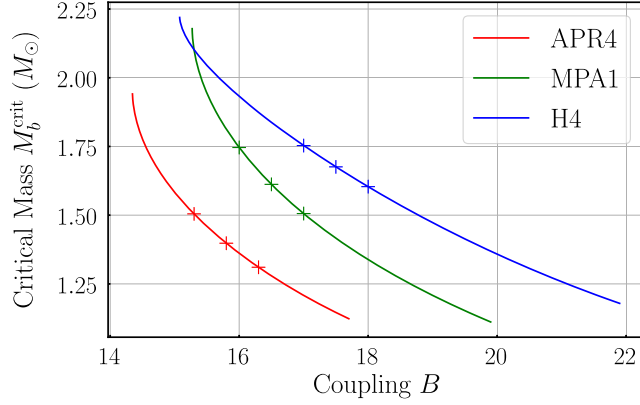
FIG. 1. Critical baryon rest mass of NSs that are marginally scalarized when isolated as functions of the coupling constant B for $m_\phi = 1.33 \times 10^{-11}$ eV. The plus markers indicate the coupling strength which we choose to generate the mass sequences for each EOS.

to investigate different outcomes of postmerger remnants. Each model is referred to in the manner of the example: `MPA1_B16.5_M1.70` corresponds to the equal-mass binary with the MPA1 EOS, $B = 16.5$, and $M_b = 1.70 M_\odot$ for an individual NS. Since the coupling strengths considered are not very strong, the ADM mass ($M_{\rm ADM}$) of the isolated NS deviates only slightly ($\lesssim 10^{-3} M_\odot$) from the star having the same baryon mass in GR.

We construct the BNS initial data in a quasiequilibrium state by generalizing the public spectral code FUKA [67] to the massive DEF theory. The BNS configurations are prepared with an initial separation of 44.31 km, with which the BNS models experience 3–5 orbits before merger. Note that, in our numerical simulation, the virial error of the initial data defined by the relative difference of ADM mass and Komar mass is always smaller than 0.04%. We refer the readers to Ref. [11] for the detailed initial data formulation for constructing quasiequilibrium states of BNS in the massive DEF theory.

D. Gravitational wave extraction

The information of GWs emitted is obtained by extracting the complex Weyl scalar Ψ_4 in the local wave zone (see, e.g., [61,62,68] for details). The Weyl scalar Ψ_4 is decomposed into (l, m) modes with spin-weighted harmonics as

$$\Psi_4(t_{\rm ret}) = \sum_{l,m} \Psi_4^{l,m}(t_{\rm ret})\, {}_{-2}Y_{lm}(\theta, \phi), \qquad (23)$$

where the retarded time $t_{\rm ret}$ is defined by [62,69]

$$t_{\rm ret} := t - D - 2M_{\rm inf} \ln\left(\frac{D}{2M_{\rm inf}} - 1\right). \qquad (24)$$

Here, $M_{\rm inf} := M_{1,{\rm ADM}} + M_{2,{\rm ADM}}$ is the total ADM mass of the isolated NSs separated at spatial infinity and D is the areal radius of the extraction sphere approximated as [62]

$$D \approx R_0 \left(1 + \frac{M_{\rm inf}}{2R_0}\right)^2, \qquad (25)$$

by assuming isotropic coordinates of nonrotating black holes in the wave zone with R_0 being the corresponding coordinate radius. We evaluate Ψ_4 at the finite radius $R_0 = 480 M_\odot \approx 709$ km and then analytically extrapolate the waveform toward null infinity by Nakano's method [70–72]. We shall focus only on the dominant $(l, |m|) = (2, 2)$ mode in this work because the contribution from other higher-multipole modes is minor for the equal-mass BNSs. The harmonic mode of GWs can be evaluated by integrating $\Psi_4^{l,m}$ twice in time given by

$$
\begin{aligned}
h^{l,m}(t_{\rm ret}) &= h_+^{l,m}(t_{\rm ret}) - i h_\times^{l,m}(t_{\rm ret}) \\
&= -\int^{t_{\rm ret}} dt' \int^{t'} \Psi_4^{l,m}(t'')\, dt'' \\
&= \int df' \frac{\tilde{\Psi}_4^{l,m}(f')}{(2\pi \max(f', f_{\rm cut}))^2} e^{2\pi i f' t_{\rm ret}}, \qquad (26)
\end{aligned}
$$

where the last line shows the fixed frequency method of [73] we employed for the calculation and $f_{\rm cut}$ is the cutoff frequency set to be $0.8 M_{\rm inf}\Omega_0/(2\pi)$, with Ω_0 being the initial angular velocity of the binary obtained from the initial data. The merger time $t_{\rm merge}$ is defined at the time of the peak GW strain $h^{2,2} := h_+^{2,2} - i h_\times^{2,2}$, where $h_+^{2,2}$ and $h_\times^{2,2}$ are the plus and cross polarization of $l = m = 2$ GWs, respectively. We also calculate the instantaneous frequency $f_{\rm GW}$ of the (2, 2) mode by

$$f_{\rm GW} = \frac{1}{2\pi} \mathrm{Im}\left(\frac{h^{*2,2}\dot{h}^{2,2}}{|h^{2,2}|^2}\right), \qquad (27)$$

where the asterisk and dot symbols denote the complex conjugate and the time derivative, respectively. The interval between $t_{\rm merge}$ and the apparent horizon formation time $t_{\rm AH}$ defines the lifetime of HMNSs (i.e., $\tau_{\rm H} := t_{\rm AH} - t_{\rm merge}$), and the lifetime of the scalar cloud $\tau_{\rm S}$ is determined by the interval between the merger and the descalarization in the HMNSs (if at all).

We obtain the amplitude of the Fourier spectrum of GWs following [16,36]

$$\tilde{h}(f)^{2,2} = \sqrt{\frac{|\tilde{h}_+^{2,2}(f)|^2 + |\tilde{h}_\times^{2,2}(f)|^2}{2}}, \qquad (28)$$

from the Fourier transforms of plus $\tilde{h}_+^{2,2}(f)$ and cross $\tilde{h}_\times^{2,2}(f)$ polarization of GWs with f being the GW's

frequency. The dimensionless effective amplitude $h_{\text{eff}}(f)$ of GWs is defined by

$$h_{\text{eff}}(f) := f\tilde{h}^{2,2}(f). \tag{29}$$

The propagation group velocity of scalar waves (v_g) is stretched by m_ϕ, and the dispersion relation is given by [11,74]

$$v_g = (1 + m_\phi^2 \lambdabar_{\text{gw}}^2)^{-1/2}, \tag{30}$$

with $\lambdabar_{\text{gw}}$ being the wavelength of the scalar wave. For $\lambdabar_{\text{gw}} \gg \lambdabar_{\text{comp}}$, the speed of scalar waves is much lower than the speed of light, thus, essentially prohibiting the emission of scalar waves [75,76]. In this work, we consider a zero asymptotic value for the scalar field $(\varphi_0 = 0)$, and consequently, scalar waves do not couple to the interferometer, leaving no extra mode such as the breathing and longitude modes in emitted GWs.

III. POSTMERGER SCENARIOS

In GR, the final fate of the postmerger remnant of BNSs depends primarily on the total mass and the EOS, while the mass of dynamical ejecta and the torus formed around the postmerger black hole (if at all) should be also sensitive to the mass ratio [38,77,78]. In terms of the HMNS's lifetime, we categorize the final outcome of BNS mergers into three different scenarios:

(i) prompt collapse to black hole,
(ii) short-lived HMNS formation $(\tau_H < 10 \text{ ms})$,
(iii) long-lived HMNS formation $(\tau_H > 10 \text{ ms})$,

where the criteria of 10 ms is a subjective choice. On top of the above categorization for BNS remnants, the presence of a scalar field introduces more variety in the final states (see Fig. 2).

All the possible outcomes are showcased in Fig. 3, where the evolution of the relative difference of maximum rest-mass density

$$\delta\rho_{\max} := \rho_{\max}(t)/\rho_{\max}(t=0) - 1 \tag{31}$$

and the maximum scalar-field amplitude[1]

$$\varphi_{\text{amp}} := \text{sgn}(\varphi)\max(|\varphi|) \tag{32}$$

are plotted for four selected models with MPA1 EOS and scalar-field parameters $(B, m_\phi) = (16, 1.33 \times 10^{-11} \text{ eV})$.

---

[1]Since the change of sign of $\varphi \to -\varphi$ does not alter the evolution of the system, we adopt the convention of negative value of φ when spontaneous scalarization happens. Therefore, we flip the sign of φ in the plots if positive φ arises when the HMNS is spontaneously scalarized unless φ experiences change of sign in the scalarization/descalarization process.
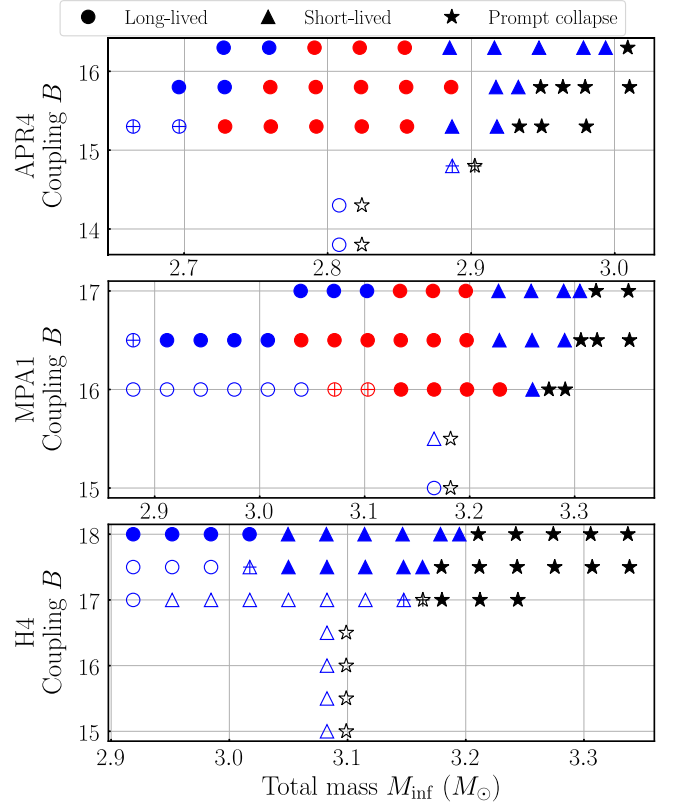

FIG. 2. Summary of all the models in this work. The circle, triangle, and black star markers represent the final fate of postmerger remnant as long-lived HMNSs, short-lived HMNSs, and prompt collapse to a black hole, respectively. The filled (respectively, hollow) markers indicate the presence (respectively, absence) of spontaneous scalarization for isolated NS, while the plus markers indicate the occurrence of dynamical scalarization. The models that undergo descalarization are marked in the red color.

We briefly summarize all the possible scenarios of the scalar-field evolution according to Fig. 3 and leave the in-depth discussion to the following sections. In the premerger phase, the scalar field can be excited if the NSs are compact enough to undergo spontaneous scalarization (blue and yellow lines) or dynamical scalarization (green line). Otherwise, the scalar field remains insignificant up to merger (red line). As we will show in Sec. III C, the scalarization history of the BNS plays an important role in the prompt collapse threshold mass. In the postmerger phase, depending on the final mass of the HMNS, it can either be spontaneously scalarized (red) or "descalarize" after a certain time to form an oscillating scalar cloud with appreciable amplitude. In the case where black holes are formed (blue and yellow), the scalar field does not dissipate away entirely, and an oscillating scalar cloud forms from the fossil scalar field instead. Although we will discuss different outcomes of BNS mergers based on the lifetimes of the HMNS and the scalar cloud, it should be noted that these timescales are not to be taken as exact for simulated
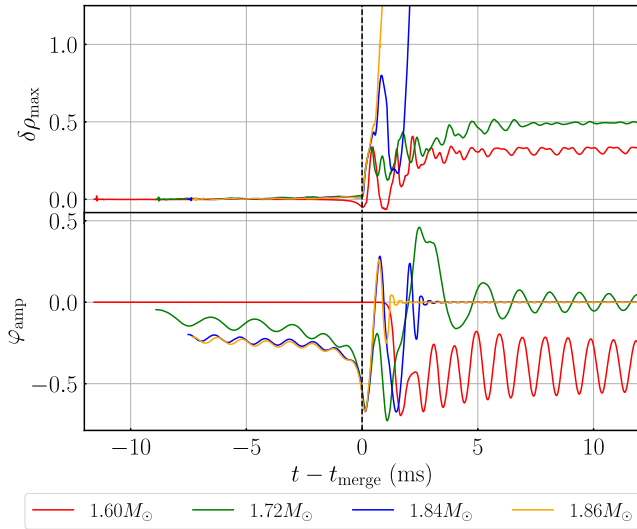
FIG. 3. Evolution of the relative difference of maximum rest-mass density $\delta\rho_{\max} := \rho_{\max}(t)/\rho_{\max}(t=0) - 1$ (top) and of the maximum scalar-field amplitude φ_{amp} (bottom) with different initial baryon rest mass of individual NSs with MPA1 EOS. The scalar-field parameters are set as $B = 16$ and $m_\phi = 1.33 \times 10^{-11}$ eV.

models. In fact, it is impossible to determine accurately the lifetimes in the numerical simulation in practice, since the HMNS after the merger is close to a marginally stable state, and any small perturbation (including numerical errors) will alter its collapse time; thus, the dynamics is extremely sensitive to the grid resolution. Thus, the values can be considered as an approximate estimate and the scenarios characterized by them are still qualitatively robust.

It can be noticed that the scalar field φ_{amp} experiences $\sim 10\%$ perturbation for scalarized binaries in the inspiral phase, which indicates that the scalar field has not yet perfectly reached the quasiequilibrium state. One possible reason is the insufficient grid resolution to resolve the exponential falloff tail of the scalar field in our initial data solver. The other possible reason is that the zero scalar-field momentum $\Phi = 0$ condition employed in our initial data formulation [11] could possibly induce some initial perturbation in the system. While any initial perturbation of the scalar field in the massless DEF theory [43,44] can freely propagate out and dissipate quickly, in the presence of nonzero scalar mass m_ϕ, perturbations with a wavelength smaller than the Compton wavelength will be trapped and remain in the vicinity of the system. Nonetheless, the initial perturbation of the rest-mass density $\delta\rho_{\max}$ is less than 1%, and hence, we believe that the effect of the scalar-field perturbation is minor.

A. Long-lived neutron star remnant

We first recap the key criterion for spontaneous scalarization in a single star following [43,45,79], which is also

useful in explaining the evolution of the scalar field in the HMNS. The onset of scalarization can be approximately described by taking the weak field limit of Eq. (6) with an average value of T within the star radius R, $\bar{T}$, as

$$(\Delta - m_\phi^2)\varphi = 2\pi B\bar{T}\varphi, \tag{33}$$

where Δ is the flat Laplacian. Denoting $k^2 := -(2\pi B\bar{T} + m_\phi^2)$, the conditions for scalarization are given as $k^2 > 0$ and $kR \to \pi/2$ for R the NS's radius [43,45]. For the case of $B > 0$ and assuming that the relativistic corrections to matter are small (i.e., $\bar{T} \sim -\rho$), scalarization is likely to happen if $\bar{T} \sim -\rho < T_{\mathrm{crit}} := -m_\phi^2/(2\pi B)$. However, scalarization is unlikely to occur if a bulk of the HMNS's interior is ultrarelativistic with $T = -\rho h + 4P > T_{\mathrm{crit}}$. The critical value of $\bar{T}$ depends on the actual profile of the star, while T_{crit} still serves as a good indicator for understanding the scalarization criterion (see below).

Shortly after the merger, an ultrarelativistic region can be formed in the HMNS for some cases, where the descalarization soon ensues. However, the core of a natal HMNS may not be in an ultrarelativistic regime even though possessing a much higher central density than that of the progenitors. In this case, scalarization may occur in the HMNS even if the progenitors remain unscalarized up to the merger (i.e., for a not-extremely-large value of B). However, the subsequent mass accretion may lead to the emergence of a region with $\bar{T} > T_{\mathrm{crit}}$, resulting in a descalarization. In the event of a *marginal* descalarization, the scalar cloud trapped by the central object oscillates with a larger amplitude than the case where the condition of $\bar{T} > T_{\mathrm{crit}}$ is conspicuously satisfied.

Before delineating different scalarization and descalarization scenarios for long-lived HMNSs in the following subsections, we demonstrate each channel by a representative model in Fig. 4, in which the snapshots of rest-mass density (left column of each panel) and scalar field (right column of each panel) on the equatorial plane in the postmerger phase are displayed. For MPA1_B16.0_M1.60, the HMNS never reaches the ultrarelativistic regime and remains scalarized until the end of the simulation, while the descalarization upon the criterion is met fully and marginally for MPA1_B17.0_M1.80 and MPA1_B16.5_M1.70, respectively.

1. Long-lived scalarized HMNS

Figure 5 shows the evolution of the maximum rest-mass density $\rho_{\max}$ and scalar-field amplitude φ_{amp} for selected models that yield a long-lived HMNS for three different EOSs. We first focus on the cases for which the HMNS confidently (solid) and marginally (dashed; present only for the H4 EOS) remains spontaneous scalarized at $t - t_{\mathrm{merge}} = 10$ ms. Some models with small values of B do not exhibit dynamical scalarization during the inspiral
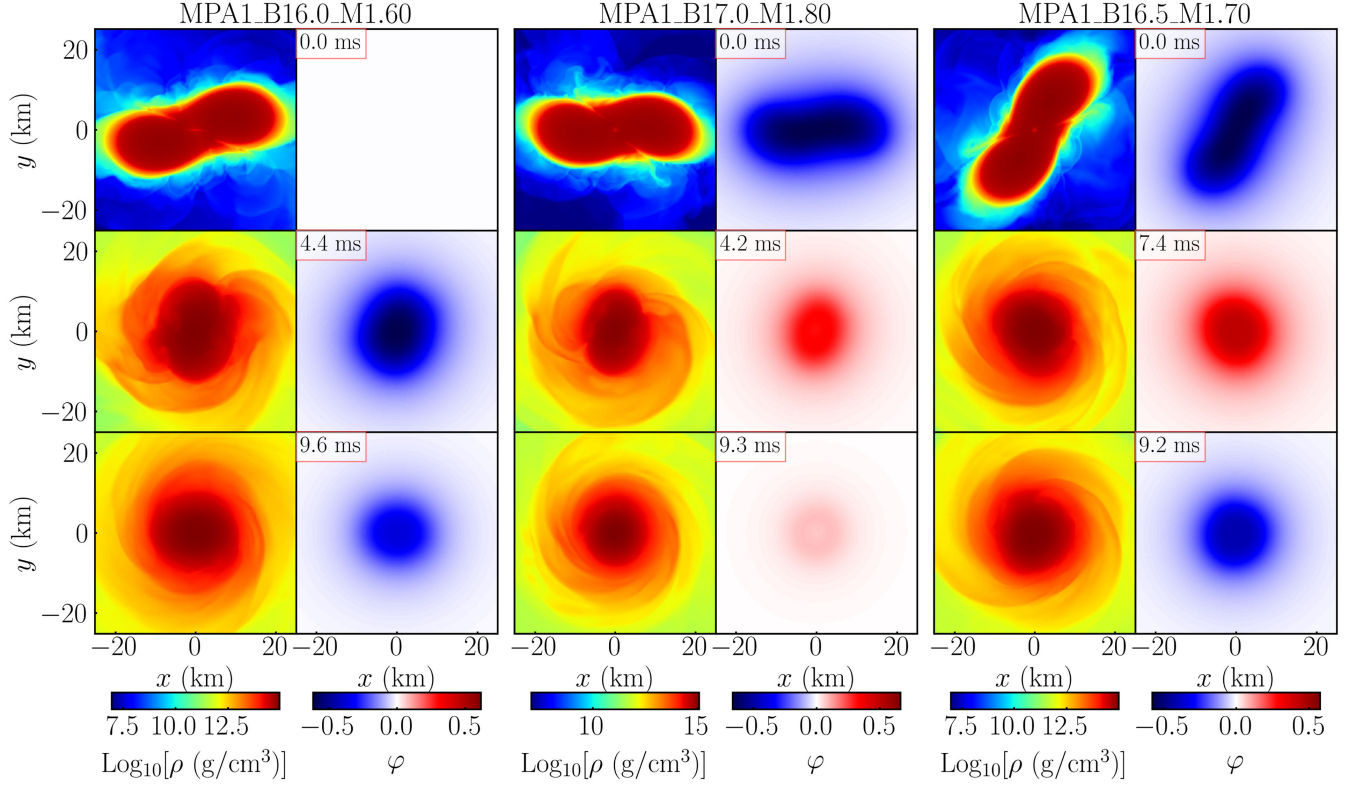
FIG. 4.   Snapshots of the rest-mass density ρ (left column of each panel) and scalar field φ (right column of each panel) on the equatorial plane for the cases of long-lived HMNS formation with the MPA1 EOS. The baryon mass M_b of each NS in units of $M_\odot$ and coupling strength B are $(M_b, B) = (1.60, 16.0)$ (left), $(M_b, B) = (1.80, 17.0)$ (middle), $(M_b, B) = (1.70, 16.5)$ (right). The time for each snapshot is indicated in the red boxes with time measured from the onset of merger.

phase, but scalarization can still occur in the postmerger phase (e.g., MPA1_B16.0_M1.60), because the HMNS has a higher compactness compared to the corresponding isolated NS, so that even for a small value of B, $\sqrt{-TR} \sim \sqrt{\rho R} \sim \sqrt{M/R}$ in the resulting HMNS can be high enough to fulfill the criterion of spontaneous scalarization.

Generally, the scalar field for scalarized HMNSs first gets amplified during merger and then settles down to a certain saturation level ($|\varphi| \sim 0.5$–0.7 in our cases) in a time interval of ~ 2 ms. The exact timescale depends on the coupling strength B; for example, the scalar field for H4_B17.5_M1.60 takes ≈ 1.7 ms to grow to the peak value after merger, while for H4_B17.0_M1.60 it takes ≈ 2.1 ms. This illustrates that it typically takes longer for the scalar field to grow to saturation for a weaker coupling, in line with the previous numerical studies where massless scalar field is considered [43].

The enhancement or activation of the scalar field during merger introduces an oscillation for it in the HMNS. Because of the nonzero mass of the scalar field, this oscillation does not dissipate quickly in contrast to the massless case [43], but instead gets trapped and persists for a timescale longer than 10 ms after the onset of merger with appreciable oscillation amplitude $\lesssim 0.1$ for φ. The oscillation frequency of the scalar field coincides with the

one for the rest-mass density at around 1 kHz. The mode associated with this pattern is believed to attribute to the radial ϕ mode since it falls in the band of a radial mode [80] of scalarized HMNSs.

For H4_B17.0_M1.60 (blue solid line), H4_B17.5_M1.64 (green dashed), and H4_B18.0_M1.66 (red dashed) in the bottom panel of Fig. 5, we find a unique feature. For these models, the scalar fields go to zero at ~ 10 ms after the onset of merger, and a black hole forms very soon afterward, as we can see that the rest-mass density is also growing rapidly. The descalarization shortly prior to the black hole formation is not triggered by the criterion $\bar{T} > T_{\text{crit}}$, but rather should be attributed to the no-hair theorem in the DEF theory (e.g., [81] and the references therein).

2. Descalarized HMNS

In this section, we pay attention to the models for which the long-lived HMNSs undergo descalarization that is induced by the secular contraction of the HMNS due to the GW emission and angular momentum redistribution via gravitational torque associated with the nonaxisymmetric structure of the merger remnant.

The dotted curves in Fig. 5 show the evolution of models that descalarize over a dynamical timescale after the onset
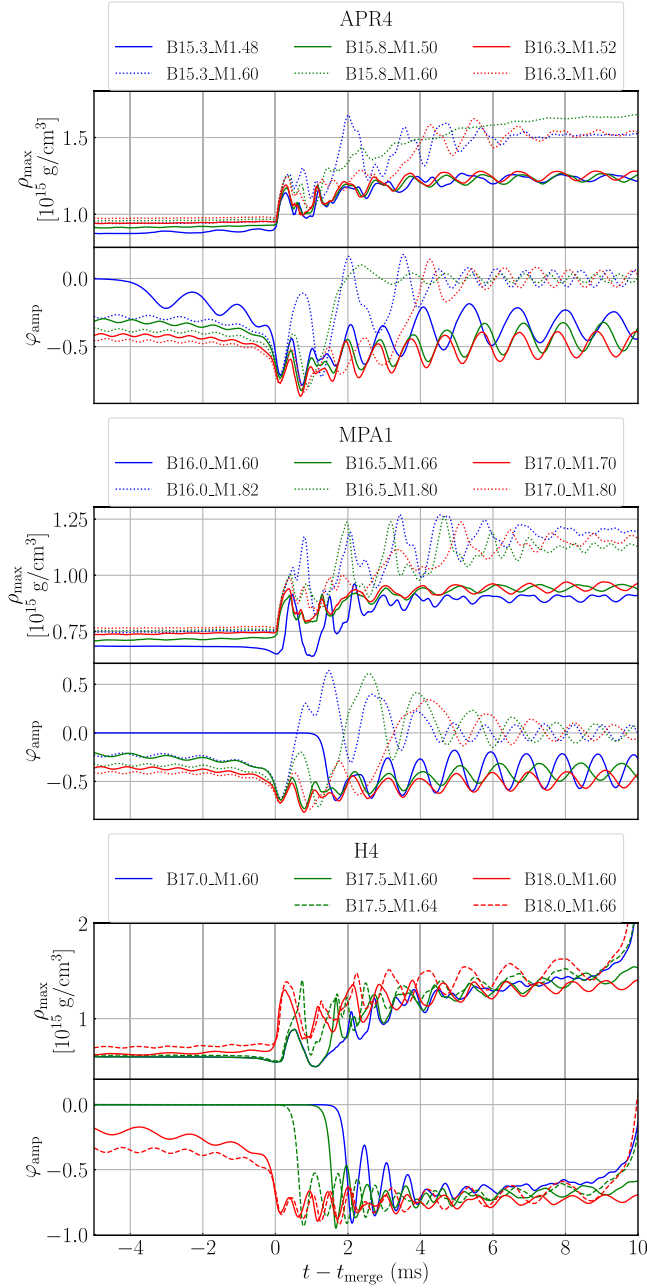
FIG. 5. Evolution of the maximum rest-mass density ρ_{max} and scalar-field amplitude φ_{amp} for the long-lived HMNS formation with APR4 (top), MPA1 (middle), and H4 (bottom) EOS. The solid and dashed curves correspond to spontaneously scalarized HMNS formation, and the dotted curves correspond to models in which descalarization happens within 10 ms after the merger.

of merger. Taking MPA1_B16.0_M1.82 as an example (blue dotted curve in the middle panel), we find that the scalar field promptly goes to zero when the maximum density rises to become ultrarelativistic during the postmerger evolution. However, the scalar field does not stop at zero, but instead forms an oscillating scalar cloud around the HMNS with an appreciable amplitude of $\lesssim 0.1$, which
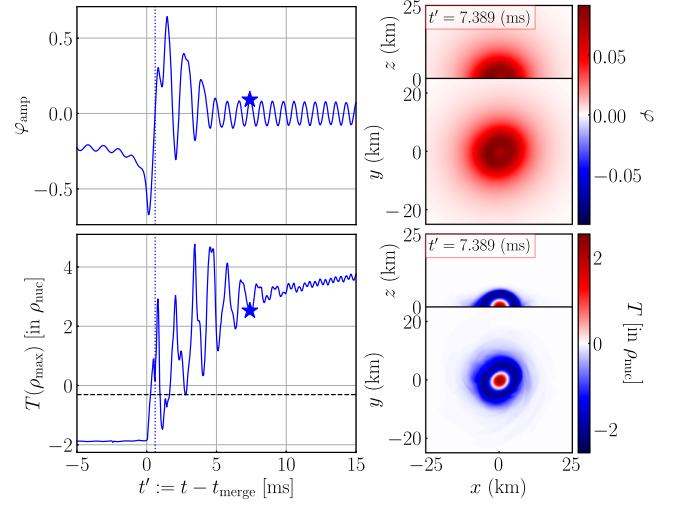

FIG. 6. For a prompt descalarization scenario MPA1_B16.0_M1.82, left panels show the evolution of the scalar-field amplitude φ_{amp} (top left) and trace of stress-energy momentum tensor $T := T^a{}_a$ (bottom left) in units of the nuclear saturation density $\rho_{nuc} = 2 \times 10^{14}$ g/cm^3 at maximum density ρ_{max} point. The blue dotted vertical line and the black dashed horizontal line show the descalarization time τ_S and the critical value T_{crit}, respectively. The blue stars indicate the time of the snapshots of φ (top right) and T (bottom right) on equatorial (x-y) and vertical (x-z) planes.

differs from the massless case in which the scalar field is completely turned off after descalarization [43]. A note is necessary here to say that the term "descalarized HMNS" does not mean the scalar field is totally dissipated, but rather, it represents an HMNS with a long-lived oscillating scalar field with the zero time-averaged value $\langle \varphi_{amp} \rangle = 0$. Owing to the residue scalar cloud, it is nontrivial to determine definitely the time when descalarization happens, and we simply define the descalarization time τ_S as the time of the first zero crossing of the scalar-field amplitude φ_{amp} during the postmerger phase.

To further understand the condition of the descalarization, we show the evolution of the scalar-field amplitude φ_{amp} together with T at the maximum density $T(\rho_{max})$ in Fig. 6 for model MPA1_B16.0_M1.82 for which the prompt descalarization happens during the postmerger phase with $\tau_S = 0.60$ ms. Here, $T(\rho_{max})$ in units of the nuclear saturation density ρ_{nuc} ($= 2 \times 10^{14}$ g/cm^3) is plotted. In the inspiral phase, the NSs are initially spontaneously scalarized which is consistent with the scalarization condition $T(\rho_{max}) < T_{crit}$ as the central value of $T \approx -2\rho_{nuc}$. Once the NSs merge, $T(\rho_{max})$ raises rapidly due to the increase in maximum density and thermal contribution from shock heating and immediately flips sign to become positive. Soon after the scalar field crosses T_{crit}, the descalarization occurs. Note that $T(\rho_{max})$ fluctuates around T_{crit} for a few times due to the radial oscillation, temporally satisfying the scalarization

condition ($T < T_{crit}$) during those cycles. As it turns out, the scalar field is likely to temporarily reach a high value, as in spontaneous scalarization, and hence introduces large oscillation after τ_S.

As $T(\rho_{max})$ shifts further away from T_{crit}, the scalar field quickly damps, leaving an oscillating scalar cloud around the HMNS. In contrast to the ϕ mode in spherical NSs in the massless DEF theory, for which the damping time of φ is $\lesssim 1$ ms [80], the residual scalar cloud persists for more than 10 ms in the massive case, forming a long-lived quasinormal mode with appreciable amplitude $\sim\mathcal{O}(0.1)$. Such a long-lived ϕ mode observed in both scalarized and descalarized cases is consistent with the results of [82], which suggests that the presence of mass term m_ϕ could significantly extend the lifetime of the radial ϕ mode in the massive Brans-Dicke scalar-tensor theory. Also shown in the right panels of Fig. 6 are the snapshots of the scalar field φ and T at 7.389 ms after the onset of merger. Despite the large value of $T \sim 2\rho_{nuc}$ at the center, which forbids the HMNS from being spontaneously scalarized, it still contains considerable matter with $T < T_{crit}$ surrounding the center, whose size is comparable to the Compton wavelength $\lambdabar_{comp} = 14.8$ km. This creates an off-centered potential well on the right-hand side of Eq. (33) and as such traps the scalar field in a hollow sphere shape as shown in Fig. 6; this is different from the scalar-field profile of spontaneous scalarized HMNSs in Fig. 4, for which the peak value of φ is located at the center of the NSs (see also [83]).

Other than the prompt descalarization scenario, the HMNS can still be subsequently descalarized due to the secular contraction. In some models shown as red dotted curves in Fig. 5, such as APR4_B16.3_M1.60 and MPA1_B17.0_M1.80, the HMNSs remain spontaneously scalarized for a few milliseconds after the onset of merger. Meanwhile, the rest-mass density ρ_{max} continues increasing due to the contraction resulting from the angular momentum dissipation by the GW emission and the angular momentum redistribution via gravitational torque associated with the nonaxisymmetric structure of the HMNS until it reaches the ultrarelativistic limit and triggers the descalarization. However, if the maximum rest-mass density of the HMNS settles down to a value very close to the critical value for scalarization, the HMNS may undergo several cycles going between states of scalarization and descalarization due to the density fluctuation caused by the radial oscillation. Figure 7 shows the evolution of maximum density ρ_{max} and scalar-field amplitude φ_{amp} for the marginally descalarized models, which are denoted as the least massive descalarized HMNS along the mass sequence. As the transition state between scalarized and descalarized HMNSs, any perturbation in density allows the HMNS to temporarily reach the scalarization criteria and drive the scalar field toward the level of the spontaneously scalarized HMNS. Different from the hollow spherical scalar clouds
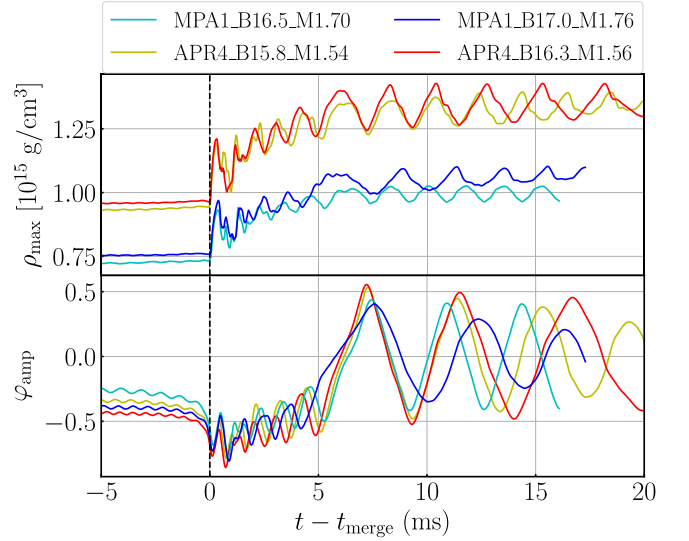

FIG. 7. Evolution of the maximum density ρ_{max} (top) and scalar-field amplitude φ_{amp} (bottom) for marginally descalarized models with APR4 and MPA1 EOSs.

formed around the descalarized HMNS, the scalar cloud's profile still peaks at the center, similar to the spontaneously scalarized models in the marginally descalarized cases as illustrated in Fig. 4 for model MPA1_B16.5_M1.70 (right panel). Therefore, it contains a much stronger oscillation in φ than for other descalarized models with the amplitude ~ 0.5.

In addition to the strong scalar-cloud oscillation, the marginally descalarized models also have a much lower frequency of ϕ mode with $\lesssim 500$ Hz. We perform Fourier transform of φ_{amp}^2 for the postmerger phase of long-lived HMNSs to obtain the characteristic frequency[2] since the scalar field enters the modified Einstein field equations, Eq. (5), as $\phi \sim \varphi^2$ and thus φ^2 is physically more relevant to hydrodynamics. Indeed, we find a better agreement between the Fourier spectrum of ρ_{max}[3] and φ_{amp}^2. To obtain a cleaner spectrum, we cut the transient evolution of the scalar field after the change of the scalarization state, which is the first 2 ms after the onset of merger for the scalarized cases, while for the descalarized cases we cut the first few milliseconds after the descalarization happened until the scalar field reaches at most twice its final amplitude.

---

[2]Note that, instead of the conventional choice φ_{amp} used in other studies [80,82], we choose specifically φ_{amp}^2 for the Fourier analysis which introduces an extra factor of 2 in frequency for the perturbation of φ if the background scalar field is zero (i.e., in the case of a descalarized HMNS with time-averaged $\langle\varphi_{amp}\rangle = 0$). However, this choice does not alter the frequency of the Fourier spectrum for the spontaneously scalarized HMNS case.

[3]While the perturbation of rest-mass density ρ is decoupled with φ in the GR branch of static spherical stars [80], the evolution of ρ would still be affected by φ even for the descalarized HMNS case in full dynamical simulation.
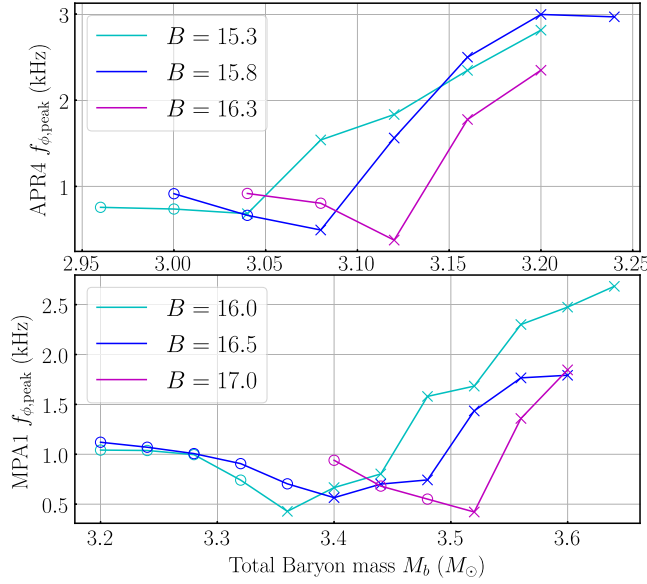
FIG. 8. The peak frequency of φ_{amp} for EOS APR4 (top) and MPA1 (bottom) with respect to the total baryon mass of the system for the long-lived HMNS scenario. The cross and circle markers indicate the models with and without descalarization, respectively.

Denoting $f_{\phi,peak}$ as the peak frequency of the Fourier spectrum of φ_{amp}^2, which is believed to be the ϕ mode of the HMNS, Fig. 8 summarizes how $f_{\phi,peak}$ varies along the mass sequence for the APR4 and MPA1 EOSs, for which a descalarized HMNS can be formed. The cross and circle markers indicate the models with and without descalarization, respectively. As the total baryon rest mass of the scalarized HMNS increases, $f_{\phi,peak}$ drops and eventually reaches its minimum at the marginally descalarized models. After that, $f_{\phi,peak}$ rises along the mass sequence for the descalarized HMNS. This is consistent with the characteristics of ϕ mode as shown in Fig. 2(c) in [80] for which the mode frequency of the spontaneously scalarized branch first drops to zero at the bifurcation point, indicating the end of the scalarized state due to the mode instability, and then rises again in the GR branch. Therefore, we believe that the dominant mode in φ_{amp}^2 is the radial ϕ mode and the zero-frequency point of $f_{\phi,peak}$ at the marginally descalarized model indicates the bifurcation point of scalarized and GR branches.

We summarize τ_H (solid) and τ_S (dashed) for the simulated models whenever they can be determined in Fig. 9. The scalar cloud's lifetime τ_S depends strongly on the coupling strength B as shown by the dashed curves in Fig. 9. In general, τ_S is longer for the larger values of B. It is noticed that the descalarization of HMNSs only occurs in APR4 and MPA1 EOSs, while all the models with the H4 EOS (bottom panel) only descalarize right before the collapse, i.e., the lifetimes τ_H and τ_S overlapped with each other. Although we pick up weak coupling strengths that
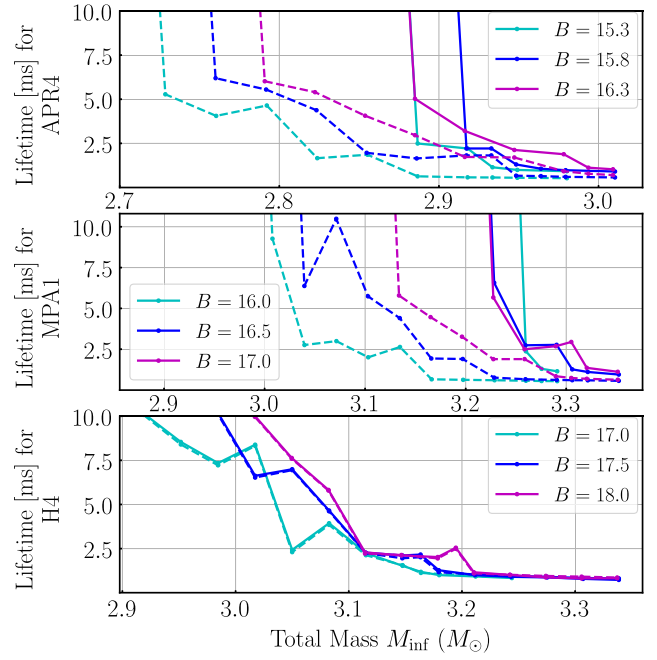

FIG. 9. Lifetimes of the excited scalar field (dashed) and HMNS (solid) for the DEF theory with $m_\phi = 1.33 \times 10^{-11}$ eV with various coupling strengths as functions of the total mass $M_{inf} := M_{ADM,1} + M_{ADM,2}$ of NSs for APR4 (top), MPA1 (middle), and H4 (bottom) EOSs.

induce the scalarization for the static spherical NSs, ranging from $B = 17$ to 18 for H4 EOS, the critical coupling strength B for the marginal scalarization decreases rapidly for more massive NSs as shown in Fig. 1. For static spherical NSs with total baryon mass greater than $2M_\odot$, spontaneously scalarization can happen for much lower coupling $B < 16$ in H4 EOS, and we expect such critical value of B could go even lower for more massive HMNSs with $M_b > 3M_\odot$. Therefore, the coupling constant B we covered is relatively strong for HMNSs, prolonging the scalarization time and thus explaining the strong scalarization behavior.

B. Delayed collapse

When the total mass of merger remnants is slightly below the threshold mass M_{thr}, the HMNS survives for a short period of time and then collapses to a black hole after subsequent angular momentum dissipation by the GW emission and angular momentum transport via the gravitational torque associated with nonaxisymmetric structure of the HMNS. We classify these delayed collapse models with $\tau_H < 10$ ms as a short-lived HMNS. We expect that the collapse could be further delayed if the HMNS is spontaneously scalarized since the scalar field will weaken the gravitational force on the surrounding matter. Figure 10 shows the evolution of ρ_{max} and φ_{amp} for short-lived HMNS models. HMNSs with the H4 EOS always remain
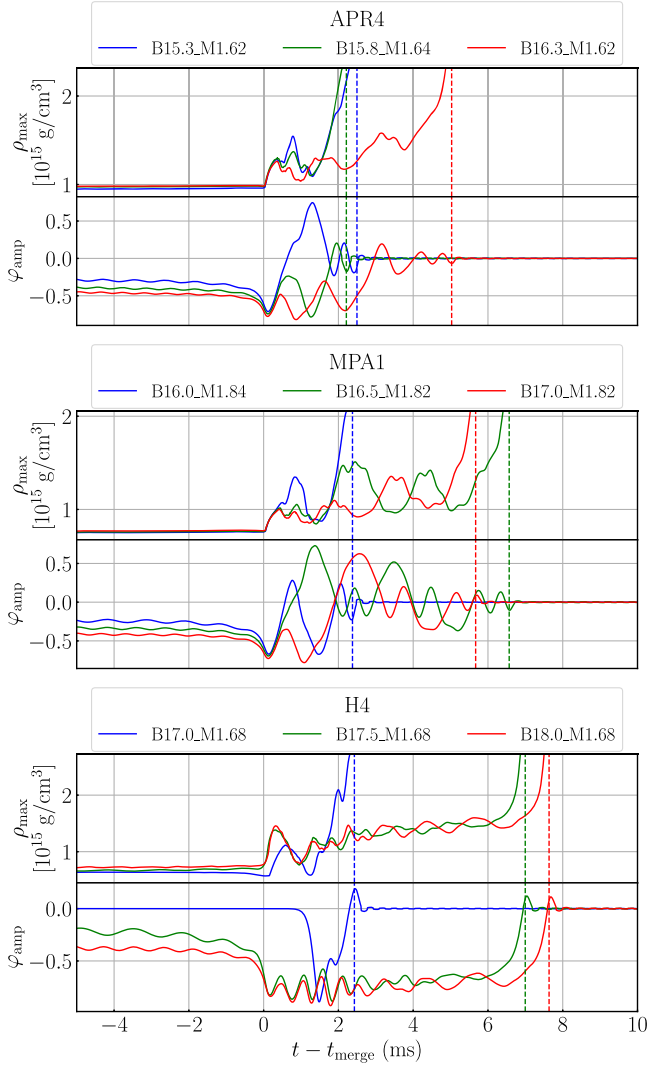
FIG. 10. Evolution of maximum density ρ_{max} (top) and scalar field amplitude φ_{amp} (bottom) for short-lived HMNS cases. The dashed line indicates the collapse time for the corresponding models.

FIG. 11. Snapshots of rest-mass density ρ and scalar field φ on the equatorial plane for a short-lived HMNS model `MPA1_B17.0_M1.82` at the onset of merger (top), before the formation of apparent horizon (middle), and at 10.9 ms after the onset of merger (bottom). The time after the onset of merger is indicated in the red box and the black filled circles plotted in the bottom panels show the location of the black hole. Notice the varying scale rule for φ in different panels.

spontaneously scalarized until the formation of a black hole because of the choice of the relatively strong coupling strength. Then, the descalarization occurs when the black hole is formed and the scalar field is quickly dissipated due to the no-hair theorem. On the other hand, HMNSs pertaining to the APR4 and MPA1 EOSs undergo descalarization earlier before the black hole formation, leaving an oscillating scalar cloud. These descalarized HMNSs have a mass $> M_{thr}^{GR}$ and yet they still survive for a few ms before forming a black hole. This indicates that the small-amplitude scalar cloud $|\varphi| \lesssim 0.1$ provides a temporal support to stave off the collapse.

Taking one particular model as an example (the same one as the red curve for MPA1 in Fig. 10), we find that the evolution of the scalar field and the HMNS in this scenario is visualized in Fig. 11 through the snapshots of the rest-mass density (left) and scalar field (right) on the equatorial
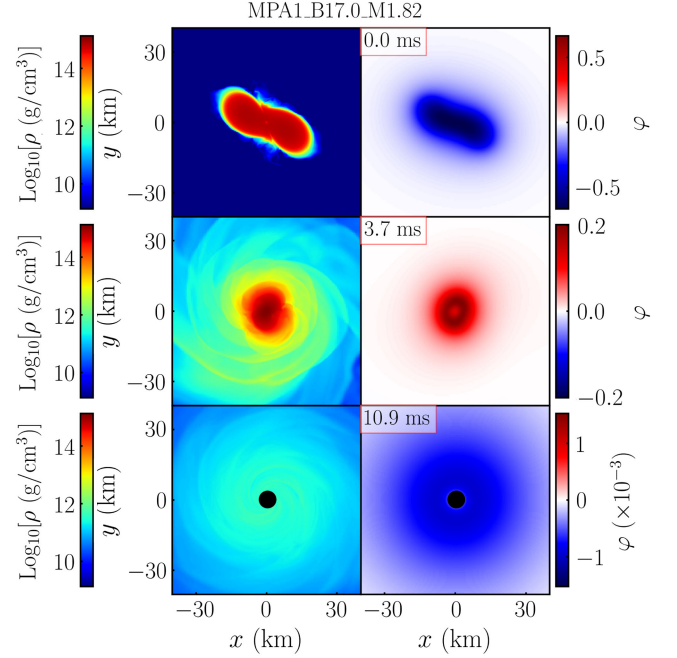
plane. The HMNS descalarizes at $\lesssim 2$ ms after the onset of merger and forms a hollow spherical scalar cloud around it (middle), similar to the scalar profile of the descalarized models (cf. Fig. 6). The scalar cloud delays the collapse of the HMNS until 5.67 ms after the onset of merger. Eventually, a black hole is formed, which is surrounded by a long-lived quasibound state of the scalar cloud with the amplitude of $\sim 10^{-4}$ (bottom) because of the nonzero mass of the scalar field (see more details in Sec. III C).

C. Prompt collapse and the threshold mass

Shortly after the fully GR BNS merger simulations were feasible, Refs. [77,84] showed that there is a mass limit on the BNSs beyond which they immediately collapse into a black hole within a dynamical timescale $\lesssim 1$ ms. In GR, the threshold mass M_{thr}^{GR} of NSs for which the prompt collapse proceeds has been vastly studied for different EOSs, whereby it was found that this threshold mass varies for different EOSs [13,21,36,39–41], but is not sensitive to the mass ratio unless the system is appreciably asymmetric as $q < 0.7$ [85]. The threshold masses for the considered EOSs, APR4, MPA1, and H4, have been found to be $2.825 M_{\odot}$, $3.225 M_{\odot}$, and $3.125 M_{\odot}$, respectively, in [86] with GR hydrodynamics simulations under conformal flatness approximation. In addition to dynamical studies,

the threshold mass can also be approximately determined by the maximum mass of differentially rotating NSs along a constant angular momentum sequence for a given EOS, i.e., the turning-point criteria is approximately valid to a large extent, provided that the rotational law can be phenomenologically modeled [87–89]. However, in the DEF theory, there could emerge a scalarized branch of equilibrium under the same EOS, angular momentum, and rotational law. The presence of the scalar field in spontaneously scalarized NS will effectively increase the stiffness of the EOS, providing additional support against gravitational collapse and thus the maximum achievable on the scalar branch has been shown to exceed that on the GR sequence [83]. This suggests the existence of HMNSs heavier than the prompt collapse threshold in GR, i.e., the final remnant with mass greater than M_{thr} in GR may not undergo prompt collapse if it is scalarized.

In practical simulations, there is no clear criterion to classify the outcome as the prompt collapse scenario. Some studies [36] used the monotonically increasing feature of ρ_{max} after the onset of merger as an indication of the prompt collapse, while some used the monotonically decreasing feature of the minimum value of the lapse function α_{min} toward zero as a criterion [85]. In this study, we employ the minimum lapse function α_{min} as the indicator for the prompt collapse when it decreases monotonically in the merger phase. Although α_{min} is a gauge-dependent variable, it directly reflects the geometrical property compared to the maximum rest-mass density ρ_{max} in the DEF framework since the contribution of hydrodynamics is coupled to the scalar field as $\phi^{-1}T_{ab}$ [cf. Eq. (5)]. When the remnant undergoes gravitational collapse, the scalar field $|\varphi|$ drops to zero drastically due to the no-hair theorem and causes a small bump in the evolution of the rest-mass density ρ_{max}.

To better resolve the threshold mass for prompt collapse, we increase the grid resolution in the binary mass sequence such that the least massive prompt collapse model and the most massive delayed collapse model differ by $\Delta M_b = 0.02 M_\odot$ in total baryon mass (i.e., $\Delta M_b = 0.01 M_\odot$ for each NS). We define the threshold mass as $M_{\text{thr}} := (M_{\text{inf,PC}} + M_{\text{inf,SL}})/2$ following [86], in which $M_{\text{inf,PC}}$ and $M_{\text{inf,SL}}$ are the ADM masses of the least massive prompt collapse model and most massive delayed collapse model at infinite orbital separation, respectively.

Figure 12 shows the threshold mass of NSs with different values of B for the three EOSs considered. We investigate the dependence of M_{thr} on B until it reaches the minimum coupling strength B^{crit} (circle markers in Fig. 12) with which spontaneous scalarization is possible for spherically symmetric NSs as shown in Fig. 1. The shaded region indicates the error bar given by $M_{\text{inf,PC}}$ and $M_{\text{inf,SL}}$. For the weak coupling case $B \lesssim B^{\text{crit}}$, the NSs are not scalarized in the inspiral phase, and thus, the contribution of the scalar field is negligible. For this case, the resultant
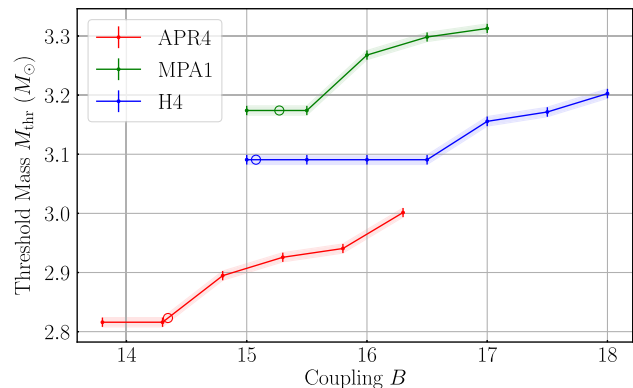

FIG. 12. Threshold mass M_{thr} for equal-mass BNSs as a function of the coupling constant B for APR4 (red), MPA1 (green), and H4 (blue) EOSs. The circle markers indicate the minimum value of the coupling strength B^{crit} with which spontaneous scalarization is possible for spherically symmetric NSs. The width of each curve reflects the bin size of the mass sampling.

threshold masses are essentially the same as in GR with $M_{\text{thr}}^{\text{GR}} = 2.816 M_\odot$, $3.174 M_\odot$, and $3.091 M_\odot$ for APR4, MPA1, and H4 EOSs, respectively. Although the obtained threshold masses $M_{\text{thr}}^{\text{GR}}$ are ~1% lower than the corresponding values found in [86], this could be due to the systematic error caused by the conformal flatness approximation employed in their study, which cannot accurately evolve spacetime with high angular momentum. This is in agreement with [40], in which the obtained M_{thr} is also lower than those in [90].

As the coupling strength B increases, the threshold mass M_{thr} begins to rise when the scalar effect becomes important. Note that whether the threshold mass M_{thr} is modified from GR is determined by scalarization history of the BNS in the inspiral phase. If spontaneous scalarization or dynamical scalarization happens before the merger, the scalar field is large enough to alter the subsequent evolution of the remnant HMNS. Otherwise, even if the final remnant could be potentially scalarized with the associated mass and angular momentum, the scalarization time is longer than the dynamical time of the remnant so that the prompt collapse can happen before the HMNS reaches a state of spontaneous scalarization. This can be found in model H4_B16.5_M1.71 shown in Fig. 13 (red), for which the scalar field grows exponentially in the merger phase, hinting at a sign of scalarization. However, the remnant undergoes prompt collapse before the scalar field is significantly amplified, and hence, the scalar effect is negligible throughout the evolution process. On the other hand, dynamical scalarization kicks in and gets saturated at 2–3 ms before merger for model APR4_B14.8_M1.62 (green in Fig. 13). Hence, the final remnant is evaded from prompt collapse with total mass of $2.887 M_\odot$ greater than threshold mass in GR $M_{\text{thr}}^{\text{GR}}$ of $2.816 M_\odot$ because
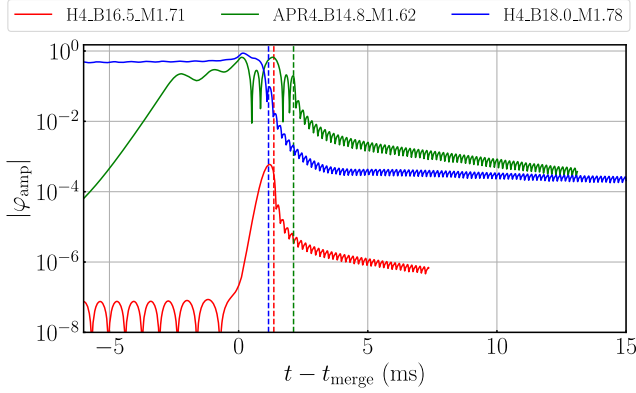
FIG. 13. Evolution of the maximum scalar-field amplitude $|\varphi_{\text{amp}}|$ for three different collapse models. The H4_B16.5_M1.71 (red) and H4_B18.0_M1.78 (blue) are prompt collapse models, while APR4_B14.8_M1.62 (green) is a delayed collapse model. The colored dotted lines show the collapse times for the corresponding models.

appreciable scalar field is built up in the inspiral phase through the scalarization process.

As mentioned in Sec. III B, after the HMNS collapses, a quasibound state of the oscillating scalar cloud will form around the black hole from the fossil scalar field if the system undergoes scalarization beforehand. Figure 13 shows that the scalar field for model H4_B18.0_M1.78 (blue) quickly dissipates most of its energy after the prompt collapse. Nonetheless, a small fraction of the original scalar field remains and settles down to a long-lived oscillating cloud with the amplitude $\sim 10^{-4}$. The final scalar cloud contains dominantly a monopole component as illustrated in the bottom panels of Figs. 11 and 14.

IV. PROPERTIES OF REMNANTS

A. Dynamical ejecta

First, we briefly discuss the material ejected from the BNS merger in the DEF theory.

One common method to identify the unbounded fluid element is to use geodesic criteria $u_t \leq -1$ for particles moving on ballistic trajectories [37,91–94]. We define the total baryon rest mass M_{ej}, total energy E_{ej}, and total internal energy U_{ej} of the ejected material by

$$M_{\text{ej}}(t) := \int_{u_t \leq -1} \rho u^t \sqrt{-g} d^3 x, \tag{34}$$

$$E_{\text{ej}}(t) := \int_{u_t \leq -1} T_{\mu\nu} n^\mu n^\nu \sqrt{\gamma} d^3 x, \tag{35}$$

$$U_{\text{ej}}(t) := \int_{u_t \leq -1} \rho u^t \epsilon \sqrt{-g} d^3 x \tag{36}$$

and approximate the kinetic energy T_{ej} as
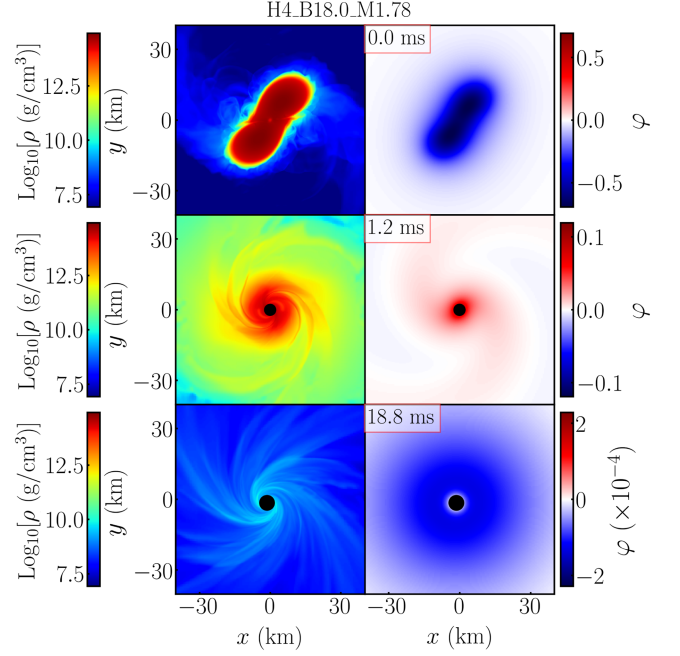

FIG. 14. Snapshots of rest-mass density ρ and scalar field φ on the equatorial plane for a prompt collapse model H4_B18.0_M1.78 at three different time slices. The time after the onset of merger is indicated in the red box and the black filled circles denote the black hole.

$$T_{\text{ej}}(t) := E_{\text{ej}} - M_{\text{ej}} - U_{\text{ej}}. \tag{37}$$

Assuming that the ejecta has nonrelativistic motion, we then estimate the average velocity v_{ej} of it as [37]

$$v_{\text{ej}}(t) := \sqrt{\frac{2T_{\text{ej}}}{M_{\text{ej}}}}. \tag{38}$$

However, the influence of gravitational potential still remains in T_{ej} as evaluated within the computation domain $\lesssim 7500$ km, hence overestimating the ejecta velocity. We therefore further estimate the extrapolated velocity $v_{\text{ej,ex}}$ following [95,96] as

$$v_{\text{ej,ex}}(t) := \sqrt{v_{\text{ej}}^2 - 2\frac{M_{\text{inf}}}{v_{\text{ej}} \times (t - t_{\text{merge}})}}, \tag{39}$$

where v_{ej} is evaluated at time t. In this paper, we define the mass M_{dyn} and the average velocity v_{dyn} of unbounded dynamical ejecta at 10 ms after the onset of merger from M_{ej} and $v_{\text{ej,ex}}$, respectively. Note that, due to the residual eccentricity $e \sim 10^{-2}$ in our simulations and limited grid resolution, the total mass of the ejected material could be altered by $\mathcal{O}(10\%)$ compared to circular orbits [97].

Figure 15 summarizes the total mass M_{dyn} and extrapolated average velocity v_{dyn} of the dynamical ejecta.
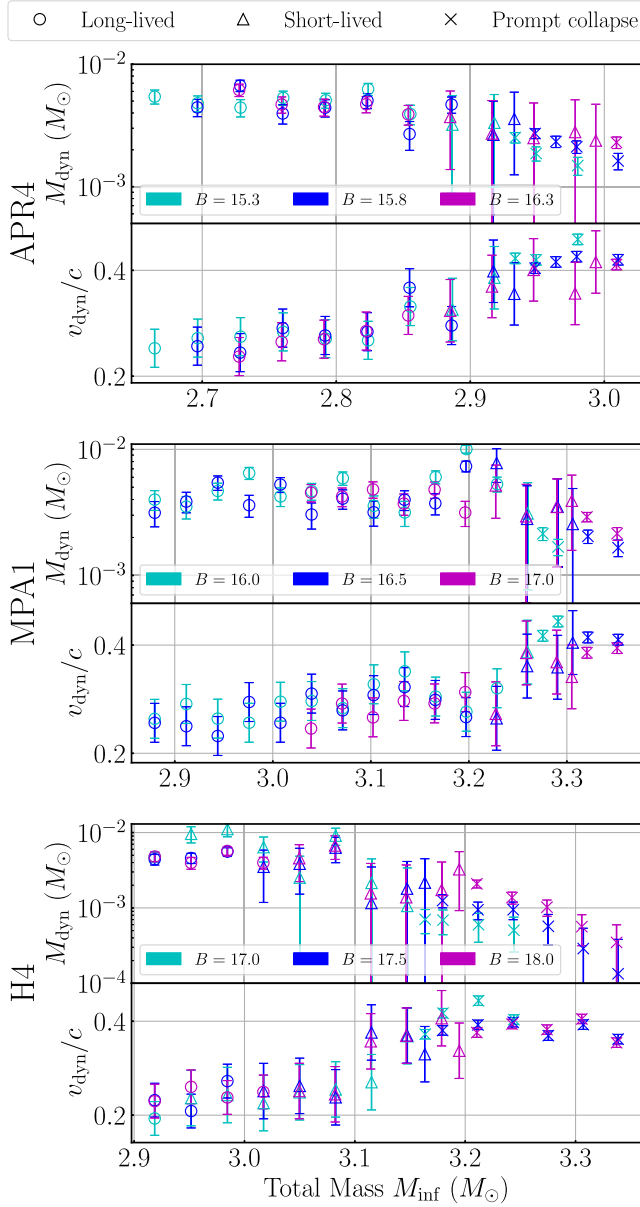
FIG. 15. Dynamical ejecta mass ($M_{\rm dyn}$) and extrapolated average velocity ($v_{\rm dyn}$) as functions of mass $M_{\rm inf}$ for all the simulated BNS models. Each panel refers to a given EOS, while different coupling strengths B are distinguished by different colors. The circle, triangle, and cross markers represent long-lived HMNS, short-lived HMNS, and prompt collapse models, respectively. The error bars are estimated from the convergence test shown in Appendix A.

The circle, triangle, and cross markers represent long-lived HMNS, short-lived HMNS, and prompt collapse models, respectively. The error bars are estimated by the convergence test for long-lived HMNSs, short-lived HMNSs, and prompt collapse cases: see Appendix A. Since the collapse time is very sensitive to the grid resolution in the short-lived HMNS formation and hence alters the final ejecta properties, the corresponding error bar is much larger than the

other two cases. The ejecta mass $M_{\rm dyn}$ falls in the range of 10^{-3}–$10^{-2} M_\odot$ depending on the EOS for the long-lived HMNS formation case with the average velocity $v_{\rm dyn} \sim 0.2c$–$0.3c$. The ejecta mass is found to be often very low as $\lesssim 10^{-3} M_\odot$ for the prompt collapse case (in particular, for the H4 EOS) due to inefficient time for outward angular momentum transport. For the APR4 and MPA1 EOSs, the ejecta mass is not extremely low as $\gtrsim 10^{-3} M_\odot$. The reason for this is that we pay particular attention to the BNS mass that is close to the threshold of the prompt collapse, and thus, shock heating effects at the merger induce a certain amount of the dynamical mass ejection. For these models, the ejecta velocity becomes fairly high $0.3 - 0.4c$ because the shock heating is the dominant source of the dynamical mass ejection.

We find that the ejecta properties are determined primarily by the lifetime of HMNSs, while the scalar effect is minor for the long-/short-lived HMNS formation case. This is reasonable because the dynamical ejecta quickly escapes the Compton wavelength $\lambda_{\rm comp} \approx 15$ km of the scalar field, and hence, the ejecta evolution is not significantly influenced by the scalar effect. This picture may change for lower values of m_ϕ, while observationally allowed values of B will be further bounded to lower values.

B. Black hole and disk

For models that undergo gravitational collapse to a black hole, we estimate the parameters of the black hole from the equatorial circumferential radius $C_{\rm e}$ and the area $A_{\rm AH}$ of the apparent horizon by assuming that the spacetime is approximately stationary with negligible effect from the matter. The black hole's mass $M_{\rm BH}$ and dimensionless spin parameter $\chi_{\rm BH}$ can be approximately computed via [98]

$$M_{\rm BH} = \frac{C_{\rm e}}{4\pi}, \tag{40}$$

$$\chi_{\rm BH} = \sqrt{1 - \left(\frac{A_{\rm AH}}{8\pi M_{\rm BH}^2} - 1\right)^2}, \tag{41}$$

respectively. Here, we evaluate $M_{\rm BH}$ and $\chi_{\rm BH}$ at 10 ms after the apparent horizon is formed. The total bounded baryon rest mass outside the apparent horizon is determined via

$$M_{\rm disk}(t) := \int_{r>r_{\rm AH}} \rho u^t \sqrt{-g} d^3 x - M_{\rm ej}(t), \tag{42}$$

with $r_{\rm AH} = r_{\rm AH}(\theta, \phi)$ being the coordinate radius of the apparent horizon. We also refer to the final disk mass $M_{\rm disk,0}$ as $M_{\rm disk}(t - t_{\rm AH} = 10$ ms$)$, where we recall that $t_{\rm AH}$ is the first formation time of the apparent horizon.

We summarize the properties of the black hole (BH) and disk in Fig. 16 for short-lived HMNS formation and prompt collapse models. For the prompt collapse models
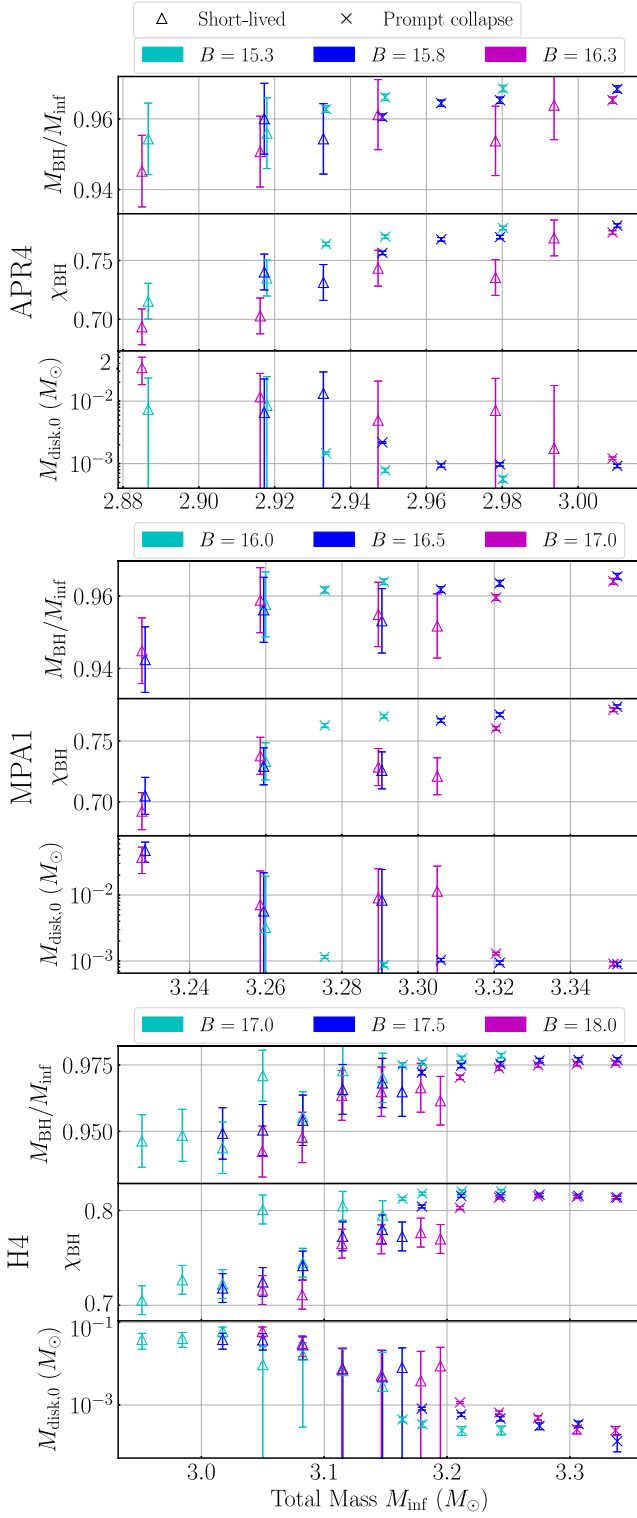
FIG. 16. Summary of final black hole and disk properties for short-lived HMNS formation (dot markers) and prompt collapse (cross markers) cases with APR4 (top), MPA1 (middle), and H4 (bottom) EOSs. For each EOS subplot, the black hole mass scaled by the total mass $M_{\rm BH}/M_{\rm inf}$ (top), dimensionless spin parameter $\chi_{\rm BH}$ (middle), and the final disk mass $M_{\rm disk,0}$ (bottom) are shown. The error bars are estimated from the convergence test shown in Appendix A.

(cross markers), the remnant disk mass is significantly suppressed with $M_{\rm disk,0} \lesssim 10^{-3} M_\odot$ due to the insufficient time for angular momentum to be transported outward and hence most of the matter falls into the BH as shown by the relatively high $M_{\rm BH}/M_{\rm inf}$ factor and dimensionless spin parameter $\chi_{\rm BH}$. Nonetheless, the dynamical timescale for the remnant to collapse to a black hole is slightly extended for larger values of B due to the decrease in compactness of isolated NSs. For example, the lifetime $\tau_{\rm H}$ rises from 0.83 ms in H4_B17.0_M1.80 to 1.01 ms in H4_B18.0_M1.80 as the coupling strength B is increased from 17 to 18. As a result, more matter remains outside the black hole, yielding a slight decrease in $M_{\rm BH}$ and $\chi_{\rm BH}$.

For the short-lived HMNS formation case, the disk mass is much higher than for the prompt collapse case and typically falls in the range of $\sim 10^{-2}$–$10^{-3} M_\odot$. Simultaneously, the resultant black hole mass and spin are lower. This result is consistent with that found in GR hydrodynamics; the lifetime of the HMNS primarily determines the final disk mass in the case of equal-mass BNSs. Since $M_{\rm thr}$ could be modified for large enough values of B in the DEF theory, the disk mass could be significantly modified compared to in GR with the same value of $M_{\rm inf}$.

Figure 17 shows the snapshots of the disk on the x-z plane at 10 ms after the formation of the apparent horizon for MPA1_B16.0_M1.86 and MPA1_B17.0_M1.86.
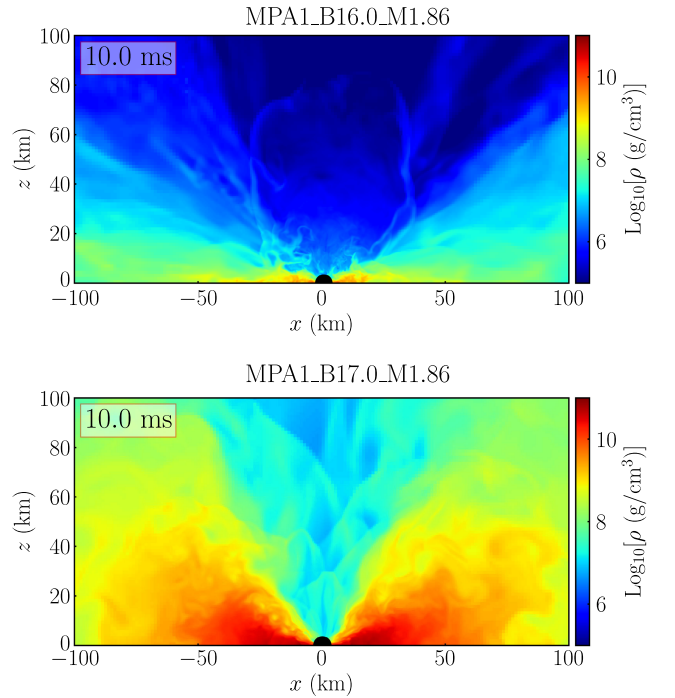

FIG. 17. Snapshots of rest-mass density ρ on the x-z plane for a prompt collapse model MPA1_B16.0_M1.86 (top) and a short-lived HMNS formation model MPA1_B17.0_M1.86 (bottom) at 10 ms after the formation of apparent horizon. The black filled circles at the center denote the black hole.
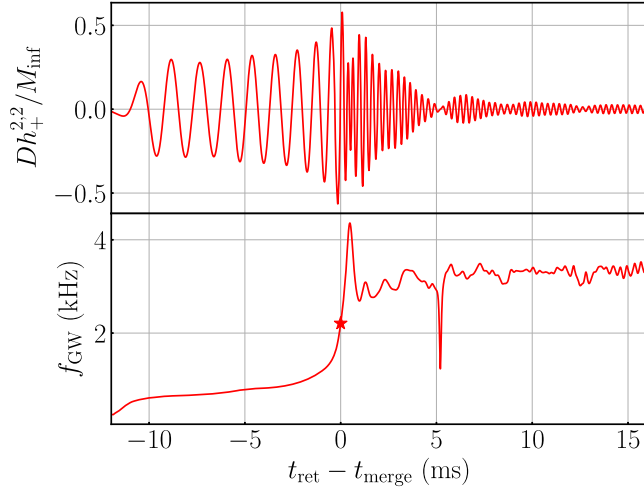
FIG. 18. GWs emitted by `APR4_B15.8_M1.56`. Top: the plus h_+ (red) polarization of GWs normalized by the extraction radius $D = 480 M_\odot$ and initial ADM mass of BNSs M_{inf} as a function of retarded time $t_{\text{ret}} - t_{\text{merge}}$. Bottom: the instantaneous GW frequency f_{GW}. The red star marker indicates the merge frequency f_{merge}.

Despite their similar masses M_{inf} ($\Delta M_{\text{inf}} < 0.002 M_\odot$), the short-lived HMNS formation model `MPA1_B17.0_M1.86` has a thick torus with mass $M_{\text{disk},0} = 7.3 \times 10^{-3} M_\odot$ outside the horizon, while only a thin disk with tiny mass $M_{\text{disk},0} = 5.1 \times 10^{-4} M_\odot$ remains in the black hole's proximity for the prompt collapse model `MPA1_B16.0_M1.86`.

C. Characteristics of gravitational waves from descalarized HMNS

In this paper, we focus on the discussion for a property of postmerger waveforms that is special to the scenarios involving a descalarization, while leaving more extensive investigation about other scenarios to a future paper [99]. Taking model `APR4_B15.8_M1.56` as an example, Fig. 18 shows the plus polarization (top) and simultaneous frequency [Eq. (27); bottom] of the GW signal. We denote the instantaneous frequency at the onset of merger at which the absolute amplitude $|h|$ reaches its maximum as f_{merge}, which is sometimes denoted as f_{peak} or $f_{2,\text{max}}$ in the literature. We also define $f_{2,\text{peak}}$ as the frequency as the dominant peak in the Fourier spectrum of h_{eff} in the postmerger phase, which is attributed to the $l = m = 2$ mode of the HMNS [15,36,100–103]. The acceleration spectral density (ASD) $\tilde{h}\sqrt{f}(\text{Hz}^{-1/2})$ is plotted in Fig. 19 for this model assuming a source distance of 50 Mpc. Since the HMNS in this model undergoes descalarization at 5.6 ms after the onset of merger, we perform the Fourier

FIG. 19. ASD $\tilde{h}\sqrt{f}$ (Hz$^{-1/2}$) of `APR4_B15.8_M1.56` at a distance of 50 Mpc. The black dashed curve indicates the ASD of the whole waveform and the vertical red dashed line indicates the $f_{2,\text{peak}}$. The blue line in the upper and lower panels shows, respectively, the ASD of the waveform before and after the onset of descalarization (5.6 ms after merge).

analysis of the waveform within two different time segments before and after descalarization indicated by the solid blue curves on the top and bottom panels in Fig. 19, respectively, while the spectrum of the whole waveform is shown by the black dashed curve. By comparing the spectrum of the whole waveform to that of the two time windows, we find that the $f_{2,\text{peak}}$ is determined primarily by the state of the HMNS at a few milliseconds after the onset of merger. In the later time window, we find an upwind shift in $f_{2,\text{peak}}$ after the descalarization since the compactness of the HMNS increases during this process. Both the increased compactness and the higher $f_{2,\text{peak}}$ are similar characteristics of the GW signature shared with the influence of a phase transition from confined hadronic matter to deconfined quark matter (e.g., [104–107]).

For comparison, we show in Fig. 20 the ASD in two time segments separated by 5 ms after the onset of merger for model `H4_B18.0_M1.64`, whereas the remnant HMNS remains scalarization in the postmerger phase. The $f_{2,\text{peak}}$ does not shift in the absence of a state transition in the HMNS throughout the postmerger phase, which verifies that the shift in $f_{2,\text{peak}}$ is indeed caused by the state transition of descalarization.
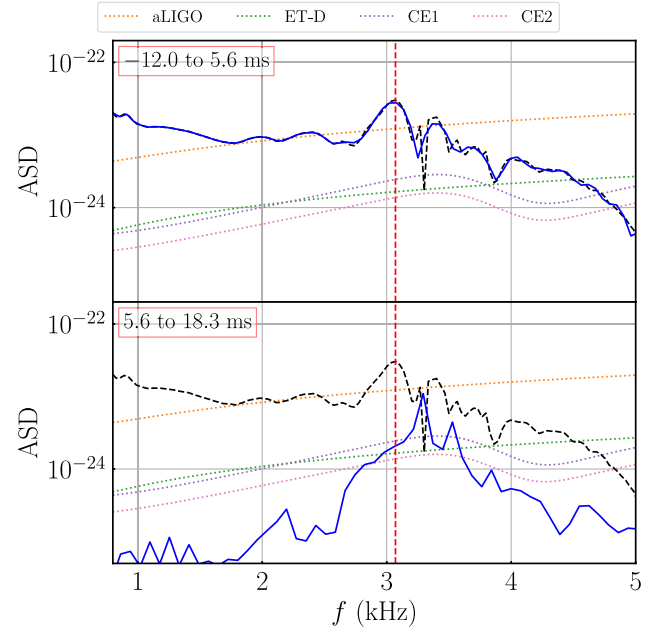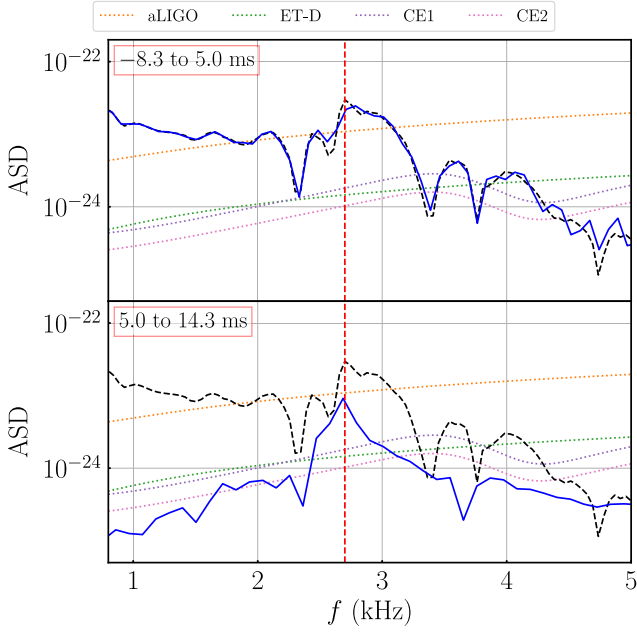
FIG. 20. ASD $2\tilde{h}\sqrt{f}$ (Hz$^{-1/2}$) of H4_B18_M1.64 at a distance of 50 Mpc. The black dashed curve indicates the ASD of the whole waveform and the vertical red dashed line indicates the $f_{2,\text{peak}}$. The blue line in the upper and lower panels shows, respectively, the ASD of the waveform before and after $t - t_{\text{merge}} = 5$ ms.

V. SUMMARY AND DISCUSSION

We performed numerical relativity simulations to study the properties of postmerger remnants and GW emission from BNS mergers in the DEF theory with a massive scalar field. We focused on a canonical scalar mass of $m_\phi = 1.33 \times 10^{-11}$ eV suggested in [11] to explore a wide range of NS mass and coupling strength B for the APR4, MPA1, and H4 EOSs. In the framework of the DEF theory, a scalar cloud can be induced in NSs and HMNSs by spontaneous scalarization or through dynamical scalarization in the binary system. This additional scalar field modifies the classic picture of BNS postmerger remnants. In the presence of scalarization, the lifetime of the HMNSs is prolonged due to the extra support from the scalar field. This raises the threshold mass for the prompt collapse by 0.1–0.2$M_\odot$, which depends on the EOS (Fig. 12).

For lower BNSs from which a long-lived HMNS is formed, the excited scalar field also changes its dynamics the from GR one. We find that the remnant can undergo descalarization if the maximum density reaches a certain critical value to become ultrarelativistic (Fig. 6), either due to the merger or subsequent postmerger evolution by the GW emission and the angular momentum redistribution via gravitational torque associated with the nonaxisymmetric structure of the remnant. Afterward, an oscillating scalar cloud remains in the vicinity of the descalarized HMNS and lasts over 10 ms after descalarization with appreciable

amplitude $\Delta\varphi \lesssim 0.1$ (Figs. 5 and 7) instead of rapidly dissipating away as would happen for a massless scalar field. Not only in a descalarized HMNS can we observe a long-lived ϕ mode. Even for HMNSs that remain scalarized to the end of the simulation, the ϕ mode excited during merger is exhibited (Fig. 5) and helps enhance a quasiradial oscillation in the HMNS. Such a long-lived scalar cloud can also be found even after the HMNS collapses to a black hole, while with much smaller amplitude (Fig. 13).

The scalar field alters the lifetime of HMNSs (Fig. 9), which in turn modifies the dynamical ejecta mass and disk mass. This may give a different kilonova signature from the GR prediction for a system with the same mass. We also observe an upward shift in $f_{2,\text{peak}}$ frequency in the postmerger GW signal due to the transition in the HMNS's state caused by descalarization (Fig. 19), which assembles the characteristics of the EOS phase transition when deconfined quark matter is revealed. The result for more detailed analysis of gravitational waveforms and their spectra will be presented in a separate paper.

ACKNOWLEDGMENTS

APPENDIX A: CONVERGENCE TEST

We summarize the details of numerical setup used in the simulations in Table I. We adopt $N = 94$ as the standard resolution throughout this paper.

Figure 21 shows a result of the convergence test considering models of long-lived HMNSs MPA1_B16.5_M1.76 [Fig. 21(a)], short-lived HMNSs MPA1_B16.5_M1.82 [Fig. 21(b)], and prompt collapse MPA1_B16.5_M1.88 [Fig. 21(c)] with three different grid resolutions as $N = (110, 94, 78)$. We obtain convergent result in the inspiral phase, while the poor resolution in the postmerger

TABLE I. Numerical setups for the simulations. The grid number for covering one positive direction (N), grid spacing in the finest refinement level (Δx), total size of computation domain $[-L, L]$, total number of moving boxes (n_{fix}) and fixed (nonmoving) boxes (n_{fix}), total number of refinement depths (d), and the extraction radius (r_{ex}).

N	Δx (m)	L (10^6 m)	n_{mv}	n_{fix}	d	r_{ex} (km)
78	189	7.56	8	6	10	709
94	157	7.56	8	6	10	709
110	134	7.56	8	6	10	709
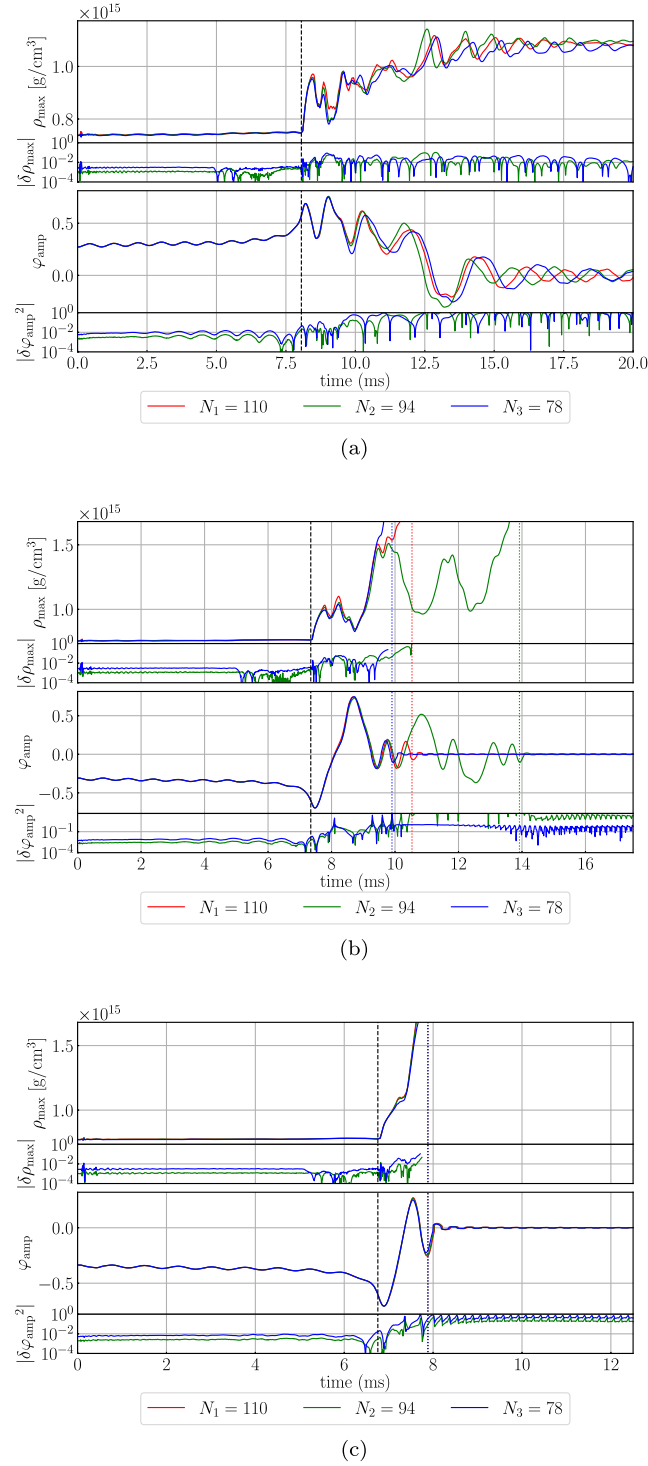
FIG. 21. Convergence test for three different models. In each subplot, the upper panel shows the evolution of maximum density ρ_{max} with resolution $N_1 = 110$ (red), $N_2 = 94$ (green), and $N_3 = 78$ (blue), together with the relative error $|\delta\rho_{max}| := |\rho_{max}/\rho_{1,max} - 1|$ in $N_{2,3}$ with respect to the highest resolution $\rho_{1,max}$. The lower panel shows the evolution of scalar field φ_{amp} and the relative error $|\delta\varphi_{amp}^2| := |\varphi_{amp}^2/\varphi_{1,amp}^2 - 1|$ in the corresponding resolutions. The black dashed line shows the merger time in N_1, while the colored dotted lines in (b) and (c) show the collapse time in different resolutions respectively. (a) Long-lived HMNS MPA1_B16.5_M1.76. (b) Short-lived HMNS MPA1_B16.5_M1.82. (c) Prompt collapse MPA1_B16.5_M1.88.

TABLE II. Errors of remnant properties for long-lived HMNSs, short-lived HMNSs, and prompt collapse cases.

Models	$\Delta M_{dyn}\ 10^{-4} M_\odot$	$\Delta v_{dyn}\ 10^{-2}$	$\Delta M_{disk} M_\odot$	$\Delta M_{BH}\ 10^{-3} M_\odot$	$\Delta \chi_{BH}\ 10^{-3}$
Long-lived HMNS	2.5	1.0	$\cdots$	$\cdots$	$\cdots$
Short-lived HMNS	23.3	5.9	5.9×10^{-5}	2.7	1.5
Prompt Collapse	7.1	3.6	1.6×10^{-2}	29.2	15.2

phase becomes notable in the presence of shocks. In particular, for the short-lived HMNS formation model `MPA1_B16.5_M1.82` [Fig. 21(b)], ρ_{max} and φ_{amp} deviate significantly at 2 ms after the onset of merger with nonconverging collapse time since the evolution of the marginally stable HMNS is extremely sensitive to the grid resolution. Nonetheless, we find consistent evolution of ρ_{max} and φ_{amp} for the cases of long-lived HMNS formation model `MPA1_B16.5_M1.76` [Fig. 21(a)] and prompt collapse model `MPA1_B16.5_M1.88` [Fig. 21(c)]. In addition, the descalarization time τ_S and the collapse time in `MPA1_B16.5_M1.76` and `MPA1_B16.5_M1.88`, respectively, have a good convergence. This indicates that

the standard resolution $\Delta x = 157$ m we employed throughout this paper is acceptable to explore the scenarios of long-lived HMNS formation and prompt collapse.

We estimate the errors of dynamical ejecta mass M_{dyn} and velocity v_{dyn}, remnant disk mass M_{disk}, and black hole parameters M_{BH}, χ_{BH} by their difference under the three resolutions considered, which are given by Table II.

APPENDIX B: LIST OF THE SELECTED MODELS

In Tables III–V, we summarize the outcomes for all the models considered in this paper.

TABLE III. Summary of outcomes for the BNS mergers in the massive DEF theory with APR4 EOS. The first column lists the model name which combines EOS, coupling strength B, and baryon mass of each NS in units of $M_\odot$. The second column shows the ADM mass M_{ADM} of each isolated NS. The third column shows the state of premerger scalarization with symbols $\times$, $\triangle$, and $\bigcirc$ corresponding to no scalarization, dynamical scalarization, and spontaneous scalarization in the premerger phase, respectively. The fourth column lists the postmerger remnants with LL, SL, and PC being a long-lived HMNS, a short-lived HMNS, and prompt collapse. The last two columns summarize the lifetime of the HMNS τ_H and scalar cloud τ_S for the cases of LL and SL, with centered dots representing the absence of descalarization in the postmerger phase.

Model name	$M_{ADM}\ (M_\odot)$	Premerger φ	Fate	τ_H (ms)	τ_S (ms)
APR4_B13.8_M1.57	1.4040	$\times$	LL	> 10	$\cdots$
APR4_B13.8_M1.58	1.4119	$\times$	PC	1.13	$\cdots$
APR4_B14.3_M1.57	1.4040	$\times$	LL	> 10	$\cdots$
APR4_B14.3_M1.58	1.4119	$\times$	PC	1.13	$\cdots$
APR4_B14.8_M1.62	1.4434	$\triangle$	SL	2.13	0.52
APR4_B14.8_M1.63	1.4513	$\triangle$	PC	1.17	0.50
APR4_B15.3_M1.48	1.3323	$\triangle$	LL	> 10	$\cdots$
APR4_B15.3_M1.50	1.3483	$\triangle$	LL	> 10	$\cdots$
APR4_B15.3_M1.52	1.3643	$\bigcirc$	LL	> 10	5.28
APR4_B15.3_M1.54	1.3802	$\bigcirc$	LL	> 10	4.06
APR4_B15.3_M1.56	1.3961	$\bigcirc$	LL	> 10	4.65
APR4_B15.3_M1.58	1.4119	$\bigcirc$	LL	> 10	1.66
APR4_B15.3_M1.60	1.4276	$\bigcirc$	LL	> 10	1.86
APR4_B15.3_M1.62	1.4433	$\bigcirc$	SL	2.50	0.63
APR4_B15.3_M1.64	1.4590	$\bigcirc$	SL	2.21	0.58
APR4_B15.3_M1.65	1.4668	$\bigcirc$	PC	1.15	0.57
APR4_B15.3_M1.66	1.4746	$\bigcirc$	PC	1.00	0.55
APR4_B15.3_M1.68	1.4901	$\bigcirc$	PC	0.92	0.53
APR4_B15.8_M1.50	1.3482	$\bigcirc$	LL	> 10	$\cdots$
APR4_B15.8_M1.52	1.3641	$\bigcirc$	LL	> 10	$\cdots$
APR4_B15.8_M1.54	1.3800	$\bigcirc$	LL	> 10	6.20

(Table continued)

TABLE III. *(Continued)*

Model name	M_{ADM} ($M_\odot$)	Premerger φ	Fate	τ_{H} (ms)	τ_{S} (ms)
APR4_B15.8_M1.56	1.3959	○	LL	> 10	5.55
APR4_B15.8_M1.58	1.4116	○	LL	> 10	4.38
APR4_B15.8_M1.60	1.4274	○	LL	> 10	1.97
APR4_B15.8_M1.62	1.4430	○	LL	> 10	1.65
APR4_B15.8_M1.64	1.4586	○	SL	2.21	1.82
APR4_B15.8_M1.65	1.4664	○	SL	3.06	0.82
APR4_B15.8_M1.66	1.4742	○	PC	1.31	0.67
APR4_B15.8_M1.67	1.4820	○	PC	1.06	0.64
APR4_B15.8_M1.68	1.4897	○	PC	0.98	0.60
APR4_B15.8_M1.70	1.5052	○	PC	0.91	0.57
APR4_B16.3_M1.52	1.3638	○	LL	> 10	⋯
APR4_B16.3_M1.54	1.3796	○	LL	> 10	⋯
APR4_B16.3_M1.56	1.3954	○	LL	> 10	6.02
APR4_B16.3_M1.58	1.4112	○	LL	> 10	5.40
APR4_B16.3_M1.60	1.4269	○	LL	> 10	4.07
APR4_B16.3_M1.62	1.4425	○	SL	5.03	2.97
APR4_B16.3_M1.64	1.4581	○	SL	3.21	1.73
APR4_B16.3_M1.66	1.4736	○	SL	2.23	1.70
APR4_B16.3_M1.68	1.4891	○	SL	1.89	0.92
APR4_B16.3_M1.69	1.4968	○	SL	1.12	0.78
APR4_B16.3_M1.70	1.5045	○	PC	1.03	0.71

TABLE IV.   Same as Table III but for the MPA1 EOS.

Model name	M_{ADM} ($M_\odot$)	Premerger φ	Fate	τ_{H} (ms)	τ_{S} (ms)
MPA1_B15.0_M1.78	1.5831	×	LL	> 10	⋯
MPA1_B15.0_M1.79	1.5909	×	PC	1.18	⋯
MPA1_B15.5_M1.78	1.5831	×	SL	3.06	⋯
MPA1_B15.5_M1.79	1.5909	×	PC	1.18	⋯
MPA1_B16.0_M1.60	1.4398	×	LL	> 10	⋯
MPA1_B16.0_M1.62	1.4559	×	LL	> 10	⋯
MPA1_B16.0_M1.64	1.4719	×	LL	> 10	⋯
MPA1_B16.0_M1.66	1.4880	×	LL	> 10	⋯
MPA1_B16.0_M1.68	1.5039	×	LL	> 10	9.27
MPA1_B16.0_M1.70	1.5198	×	LL	> 10	2.76
MPA1_B16.0_M1.72	1.5357	△	LL	> 10	3.00
MPA1_B16.0_M1.74	1.5515	△	LL	> 10	2.01
MPA1_B16.0_M1.76	1.5673	○	LL	> 10	2.64
MPA1_B16.0_M1.78	1.5831	○	LL	> 10	0.66
MPA1_B16.0_M1.80	1.5987	○	LL	> 10	0.63
MPA1_B16.0_M1.82	1.6144	○	LL	> 10	0.61
MPA1_B16.0_M1.84	1.6300	○	SL	2.37	0.57
MPA1_B16.0_M1.85	1.6377	○	PC	1.30	0.56
MPA1_B16.0_M1.86	1.6455	○	PC	1.15	0.55
MPA1_B16.5_M1.60	1.4398	△	LL	> 10	⋯
MPA1_B16.5_M1.62	1.4559	○	LL	> 10	⋯
MPA1_B16.5_M1.64	1.4719	○	LL	> 10	⋯
MPA1_B16.5_M1.66	1.4879	○	LL	> 10	⋯
MPA1_B16.5_M1.68	1.5039	○	LL	> 10	⋯

(Table continued)

TABLE IV. *(Continued)*

Model name	M_{ADM} ($M_\odot$)	Premerger φ	Fate	τ_H (ms)	τ_S (ms)
MPA1_B16.5_M1.70	1.5198	○	LL	> 10	6.38
MPA1_B16.5_M1.72	1.5356	○	LL	> 10	10.5
MPA1_B16.5_M1.74	1.5514	○	LL	> 10	5.74
MPA1_B16.5_M1.76	1.5672	○	LL	> 10	4.41
MPA1_B16.5_M1.78	1.5829	○	LL	> 10	1.94
MPA1_B16.5_M1.80	1.5986	○	LL	> 10	1.90
MPA1_B16.5_M1.82	1.6142	○	SL	6.57	0.76
MPA1_B16.5_M1.84	1.6297	○	SL	2.75	0.67
MPA1_B16.5_M1.86	1.6452	○	SL	2.77	0.62
MPA1_B16.5_M1.87	1.6530	○	PC	1.27	0.61
MPA1_B16.5_M1.88	1.6607	○	PC	1.11	0.60
MPA1_B16.5_M1.90	1.6761	○	PC	0.95	0.57
MPA1_B17.0_M1.70	1.5195	○	LL	> 10	⋯
MPA1_B17.0_M1.72	1.5353	○	LL	> 10	⋯
MPA1_B17.0_M1.74	1.5511	○	LL	> 10	⋯
MPA1_B17.0_M1.76	1.5668	○	LL	> 10	5.79
MPA1_B17.0_M1.78	1.5825	○	LL	> 10	4.47
MPA1_B17.0_M1.80	1.5981	○	LL	> 10	3.27
MPA1_B17.0_M1.82	1.6137	○	SL	5.67	1.90
MPA1_B17.0_M1.84	1.6293	○	SL	2.50	1.90
MPA1_B17.0_M1.86	1.6448	○	SL	2.69	0.85
MPA1_B17.0_M1.87	1.6525	○	SL	2.95	0.74
MPA1_B17.0_M1.88	1.6602	○	PC	1.36	0.69
MPA1_B17.0_M1.90	1.6756	○	PC	1.12	0.64

TABLE V. Same as Table III but for the H4 EOS.

Model name	M_{ADM} ($M_\odot$)	Premerger φ	Fate	τ_H (ms)	τ_S (ms)
H4_B15.0_M1.70	1.5413	×	SL	3.69	⋯
H4_B15.0_M1.71	1.5494	×	PC	1.37	⋯
H4_B15.5_M1.70	1.5413	×	SL	2.59	⋯
H4_B15.5_M1.71	1.5494	×	PC	1.37	⋯
H4_B16.0_M1.70	1.5413	×	SL	2.68	⋯
H4_B16.0_M1.71	1.5494	×	PC	1.37	⋯
H4_B16.5_M1.70	1.5413	×	SL	2.84	⋯
H4_B16.5_M1.71	1.5494	×	PC	1.36	⋯
H4_B17.0_M1.60	1.4593	×	LL	> 10	⋯
H4_B17.0_M1.62	1.4758	×	SL	8.54	8.40
H4_B17.0_M1.64	1.4923	×	SL	7.35	7.22
H4_B17.0_M1.66	1.5087	×	SL	8.39	8.32
H4_B17.0_M1.68	1.5250	×	SL	2.43	2.30
H4_B17.0_M1.70	1.5413	×	SL	3.94	3.84
H4_B17.0_M1.72	1.5576	×	SL	2.24	2.13
H4_B17.0_M1.74	1.5738	△	SL	1.52	1.56
H4_B17.0_M1.75	1.5819	△	PC	1.18	1.12
H4_B17.0_M1.76	1.5899	○	PC	1.00	1.06
H4_B17.0_M1.78	1.6060	○	PC	0.92	0.95
H4_B17.0_M1.80	1.6221	○	PC	0.83	0.87
H4_B17.5_M1.60	1.4593	×	LL	> 10	⋯

(Table continued)

TABLE V. *(Continued)*

Model name	M_{ADM} ($M_\odot$)	Premerger φ	Fate	τ_{H} (ms)	τ_{S} (ms)
H4_B17.5_M1.62	1.4758	×	LL	> 10	⋯
H4_B17.5_M1.64	1.4923	×	LL	> 10	⋯
H4_B17.5_M1.66	1.5087	△	SL	6.63	6.53
H4_B17.5_M1.68	1.5250	○	SL	7.00	7.95
H4_B17.5_M1.70	1.5413	○	SL	4.66	4.62
H4_B17.5_M1.72	1.5575	○	SL	2.27	2.24
H4_B17.5_M1.74	1.5737	○	SL	2.11	1.95
H4_B17.5_M1.75	1.5817	○	SL	2.16	2.01
H4_B17.5_M1.76	1.5898	○	PC	1.27	1.16
H4_B17.5_M1.78	1.6058	○	PC	1.00	1.03
H4_B17.5_M1.80	1.6218	○	PC	0.90	0.96
H4_B17.5_M1.82	1.6377	○	PC	0.87	0.90
H4_B17.5_M1.84	1.6535	○	PC	0.78	0.83
H4_B17.5_M1.86	1.6693	○	PC	0.73	0.81
H4_B18.0_M1.60	1.4593	○	LL	> 10	⋯
H4_B18.0_M1.62	1.4758	○	LL	> 10	⋯
H4_B18.0_M1.64	1.4922	○	LL	> 10	⋯
H4_B18.0_M1.66	1.5086	○	LL	> 10	9.96
H4_B18.0_M1.68	1.5248	○	SL	7.63	7.59
H4_B18.0_M1.70	1.5410	○	SL	5.82	5.79
H4_B18.0_M1.72	1.5572	○	SL	2.29	2.22
H4_B18.0_M1.74	1.5733	○	SL	2.11	2.14
H4_B18.0_M1.76	1.5893	○	SL	2.02	1.95
H4_B18.0_M1.77	1.5973	○	SL	2.55	2.49
H4_B18.0_M1.78	1.6053	○	PC	1.16	1.10
H4_B18.0_M1.80	1.6212	○	PC	1.01	1.02
H4_B18.0_M1.82	1.6371	○	PC	0.87	0.95
H4_B18.0_M1.84	1.6528	○	PC	0.81	0.91
H4_B18.0_M1.86	1.6686	○	PC	0.82	0.86

[1] B. P. Abbott *et al.*, Phys. Rev. Lett. **119**, 161101 (2017).

[2] B. P. Abbott *et al.*, Astrophys. J. Lett. **848**, L12 (2017).

[3] B. P. Abbott *et al.*, Astrophys. J. Lett. **848**, L13 (2017).

[4] M. M. Kasliwal *et al.*, Science **358**, 1559 (2017).

[5] B. P. Abbott *et al.*, Phys. Rev. Lett. **121**, 161101 (2018).

[6] S. De, D. Finstad, J. M. Lattimer, D. A. Brown, E. Berger, and C. M. Biwer, Phys. Rev. Lett. **121**, 091102 (2018).

[7] E. Annala, T. Gorda, A. Kurkela, and A. Vuorinen, Phys. Rev. Lett. **120**, 172703 (2018).

[8] C. D. Capano, I. Tews, S. M. Brown, B. Margalit, S. De, S. Kumar, D. A. Brown, B. Krishnan, and S. Reddy, Nat. Astron. **4**, 625 (2020).

[9] T. Dietrich, M. W. Coughlin, P. T. H. Pang, M. Bulla, J. Heinzel, L. Issa, I. Tews, and S. Antier, Science **370**, 1450 (2020).

[10] J. Zhao, L. Shao, Z. Cao, and B.-Q. Ma, Phys. Rev. D **100**, 064034 (2019).

[11] H.-J. Kuan, K. Van Aelst, A. T.-L. Lam, and M. Shibata, Phys. Rev. D **108**, 064057 (2023).

[12] M. Shibata and K. Hotokezaka, Annu. Rev. Nucl. Part. Sci. **69**, 41 (2019).

[13] S. Bernuzzi, Gen. Relativ. Gravit. **52**, 108 (2020).

[14] K. Kawaguchi, M. Shibata, and M. Tanaka, Astrophys. J. **889**, 171 (2020).

[15] M. Shibata, Phys. Rev. Lett. **94**, 201101 (2005).

[16] K. Kiuchi, Y. Sekiguchi, M. Shibata, and K. Taniguchi, Phys. Rev. D **80**, 064037 (2009).

[17] K. Hotokezaka, K. Kyutoku, and M. Shibata, Phys. Rev. D **87**, 044001 (2013).

[18] M. Shibata, Phys. Rev. D **60**, 104052 (1999).

[19] T. W. Baumgarte, S. L. Shapiro, and M. Shibata, Astrophys. J. Lett. **528**, L29 (2000).

[20] M. Shibata and K. ō. Uryū, Phys. Rev. D **61**, 064001 (2000).

[21] M. Shibata and K. Taniguchi, Phys. Rev. D **73**, 064027 (2006).

[22] G. B. Cook, S. L. Shapiro, and S. A. Teukolsky, Astrophys. J. **398**, 203 (1992).

[23] G. B. Cook, S. L. Shapiro, and S. A. Teukolsky, Astrophys. J. **422,** 227 (1994).

[24] G. B. Cook, S. L. Shapiro, and S. A. Teukolsky, Astrophys. J. **424,** 823 (1994).

[25] M. Shibata, S. Fujibayashi, K. Hotokezaka, K. Kiuchi, K. Kyutoku, Y. Sekiguchi, and M. Tanaka, Phys. Rev. D **96,** 123012 (2017).

[26] L. Rezzolla, E. R. Most, and L. R. Weih, Astrophys. J. Lett. **852,** L25 (2018).

[27] N. Farrow, X.-J. Zhu, and E. Thrane, Astrophys. J. **876,** 18 (2019).

[28] T. M. Tauris, M. Kramer, P. C. C. Freire, N. Wex, H. T. Janka, N. Langer, P. Podsiadlowski, E. Bozzo, S. Chaty, M. U. Kruckow, E. P. J. van den Heuvel, J. Antoniadis, R. P. Breton, and D. J. Champion, Astrophys. J. **846,** 170 (2017).

[29] M. D. Duez, Y. T. Liu, S. L. Shapiro, and B. C. Stephens, Phys. Rev. D **69,** 104030 (2004).

[30] K. Hotokezaka, K. Kiuchi, K. Kyutoku, T. Muranushi, Y.-i. Sekiguchi, M. Shibata, and K. Taniguchi, Phys. Rev. D **88,** 044026 (2013).

[31] K. Kiuchi, Y. Sekiguchi, M. Shibata, and K. Taniguchi, Phys. Rev. Lett. **104,** 141101 (2010).

[32] S. Fujibayashi, S. Wanajo, K. Kiuchi, K. Kyutoku, Y. Sekiguchi, and M. Shibata, Astrophys. J. **901,** 122 (2020).

[33] K. Kawaguchi, S. Fujibayashi, N. Domoto, K. Kiuchi, M. Shibata, and S. Wanajo, arXiv:2306.06961.

[34] S. Curtis, P. Mösta, Z. Wu, D. Radice, L. Roberts, G. Ricigliano, and A. Perego, Mon. Not. R. Astron. Soc. **518,** 5313 (2023).

[35] L. Combi and D. M. Siegel, Astrophys. J. **944,** 28 (2023).

[36] K. Hotokezaka, K. Kyutoku, H. Okawa, M. Shibata, and K. Kiuchi, Phys. Rev. D **83,** 124008 (2011).

[37] K. Hotokezaka, K. Kiuchi, K. Kyutoku, H. Okawa, Y.-i. Sekiguchi, M. Shibata, and K. Taniguchi, Phys. Rev. D **87,** 024001 (2013).

[38] T. Dietrich, M. Ujevic, W. Tichy, S. Bernuzzi, and B. Brügmann, Phys. Rev. D **95,** 024029 (2017).

[39] A. Bauswein, T. W. Baumgarte, and H. T. Janka, Phys. Rev. Lett. **111,** 131101 (2013).

[40] S. Köppel, L. Bovard, and L. Rezzolla, Astrophys. J. Lett. **872,** L16 (2019).

[41] R. Kashyap, A. Das, D. Radice, S. Padamata, A. Prakash, D. Logoteta, A. Perego, D. A. Godzieba, S. Bernuzzi, I. Bombaci, F. J. Fattoyev, B. T. Reed, and A. d. S. Schneider, Phys. Rev. D **105,** 103022 (2022).

[42] T. Damour and G. Esposito-Farese, Classical Quantum Gravity **9,** 2093 (1992).

[43] M. Shibata, K. Taniguchi, H. Okawa, and A. Buonanno, Phys. Rev. D **89,** 084005 (2014).

[44] K. Taniguchi, M. Shibata, and A. Buonanno, Phys. Rev. D **91,** 024033 (2015).

[45] T. Kuroda and M. Shibata, Phys. Rev. D **107,** 103025 (2023).

[46] M. Shibata and T. Nakamura, Phys. Rev. D **52,** 5428 (1995).

[47] T. W. Baumgarte and S. L. Shapiro, Phys. Rev. D **59,** 024007 (1998).

[48] M. Campanelli, C. O. Lousto, P. Marronetti, and Y. Zlochower, Phys. Rev. Lett. **96,** 111101 (2006).

[49] J. G. Baker, J. Centrella, D.-I. Choi, M. Koppitz, and J. van Meter, Phys. Rev. Lett. **96,** 111102 (2006).

[50] J. S. Read, B. D. Lackey, B. J. Owen, and J. L. Friedman, Phys. Rev. D **79,** 124032 (2009).

[51] A. Akmal, V. R. Pandharipande, and D. G. Ravenhall, Phys. Rev. C **58,** 1804 (1998).

[52] H. Müther, M. Prakash, and T. L. Ainsworth, Phys. Lett. B **199,** 469 (1987).

[53] B. D. Lackey, M. Nayyar, and B. J. Owen, Phys. Rev. D **73,** 024021 (2006).

[54] F. J. Fattoyev, J. Piekarewicz, and C. J. Horowitz, Phys. Rev. Lett. **120,** 172702 (2018).

[55] H. T. Janka, T. Zwerger, and R. Moenchmeyer, Astron. Astrophys. **268,** 360 (1993).

[56] A. Bauswein, H. T. Janka, and R. Oechslin, Phys. Rev. D **82,** 084043 (2010).

[57] M. Shibata, K. Taniguchi, and K. Uryū, Phys. Rev. D **71,** 084021 (2005).

[58] E. Barausse, C. Palenzuela, M. Ponce, and L. Lehner, Phys. Rev. D **87,** 081506 (2013).

[59] C. Palenzuela, E. Barausse, M. Ponce, and L. Lehner, Phys. Rev. D **89,** 044024 (2014).

[60] N. Sennett and A. Buonanno, Phys. Rev. D **93,** 124004 (2016).

[61] T. Yamamoto, M. Shibata, and K. Taniguchi, Phys. Rev. D **78,** 064054 (2008).

[62] K. Kiuchi, K. Kawaguchi, K. Kyutoku, Y. Sekiguchi, M. Shibata, and K. Taniguchi, Phys. Rev. D **96,** 084060 (2017).

[63] K. Kiuchi, L. E. Held, Y. Sekiguchi, and M. Shibata, Phys. Rev. D **106,** 124041 (2022).

[64] F. M. Ramazanoğlu and F. Pretorius, Phys. Rev. D **93,** 064005 (2016).

[65] S. S. Yazadjiev, D. D. Doneva, and D. Popchev, Phys. Rev. D **93,** 084038 (2016).

[66] J. C. Degollado, N. Ortiz, and M. Salgado, Phys. Rev. D **110,** 084011 (2024).

[67] L. J. Papenfort, S. D. Tootle, P. Grandclément, E. R. Most, and L. Rezzolla, Phys. Rev. D **104,** 024057 (2021).

[68] K. Kiuchi, K. Kawaguchi, K. Kyutoku, Y. Sekiguchi, and M. Shibata, Phys. Rev. D **101,** 084006 (2020).

[69] K. Hotokezaka, K. Kyutoku, and M. Shibata, Phys. Rev. D **87,** 044001 (2013).

[70] C. O. Lousto, H. Nakano, Y. Zlochower, and M. Campanelli, Phys. Rev. D **82,** 104057 (2010).

[71] H. Nakano, Classical Quantum Gravity **32,** 177002 (2015).

[72] H. Nakano, J. Healy, C. O. Lousto, and Y. Zlochower, Phys. Rev. D **91,** 104022 (2015).

[73] C. Reisswig and D. Pollney, Classical Quantum Gravity **28,** 195015 (2011).

[74] J. C. Aurrekoetxea, P. G. Ferreira, K. Clough, E. A. Lim, and O. J. Tattersall, Phys. Rev. D **106,** 104002 (2022).

[75] J. Alsing, E. Berti, C. M. Will, and H. Zaglauer, Phys. Rev. D **85,** 064041 (2012).

[76] R. Rosca-Mead, U. Sperhake, C. J. Moore, M. Agathos, D. Gerosa, and C. D. Ott, Phys. Rev. D **102,** 044010 (2020).

[77] M. Shibata, K. Taniguchi, and K. Uryū, Phys. Rev. D **68,** 084020 (2003).

[78] L. Rezzolla, L. Baiotti, B. Giacomazzo, D. Link, and J. A. Font, Classical Quantum Gravity **27,** 114105 (2010).

[79] T. Damour and G. Esposito-Farese, Phys. Rev. Lett. **70,** 2220 (1993).

[80] R. F. P. Mendes and N. Ortiz, Phys. Rev. Lett. **120,** 201104 (2018).

[81] T. P. Sotiriou, Classical Quantum Gravity **32,** 214002 (2015).

[82] J. Luis Blázquez-Salcedo, F. Scen Khoo, and J. Kunz, Europhys. Lett. **130,** 50002 (2020).

[83] K. V. Staykov, D. D. Doneva, L. Heisenberg, N. Stergioulas, and S. S. Yazadjiev, Phys. Rev. D **108,** 024058 (2023).

[84] M. Shibata, K. Taniguchi, and K. Uryū, Phys. Rev. D **71,** 084021 (2005).

[85] A. Bauswein, S. Blacker, G. Lioutas, T. Soultanis, V. Vijayan, and N. Stergioulas, Phys. Rev. D **103,** 123004 (2021).

[86] A. Bauswein, S. Blacker, V. Vijayan, N. Stergioulas, K. Chatziioannou, J. A. Clark, N.-U. F. Bastian, D. B. Blaschke, M. Cierniak, and T. Fischer, Phys. Rev. Lett. **125,** 141103 (2020).

[87] J. D. Kaplan, C. D. Ott, E. P. O'Connor, K. Kiuchi, L. Roberts, and M. Duez, Astrophys. J. **790,** 19 (2014).

[88] L. R. Weih, E. R. Most, and L. Rezzolla, Mon. Not. R. Astron. Soc. **473,** L126 (2018).

[89] N. Muhammed, M. D. Duez, P. Chawhan, N. Ghadiri, L. T. Buchman, F. Foucart, P. Chi-Kit Cheong, L. E. Kidder, H. P. Pfeiffer, and M. A. Scheel, arXiv:2403.05642.

[90] A. Bauswein and N. Stergioulas, Mon. Not. R. Astron. Soc. **471,** 4956 (2017).

[91] S. Bernuzzi, M. Breschi, B. Daszuta, A. Endrizzi, D. Logoteta, V. Nedora, A. Perego, D. Radice, F. Schianchi, F. Zappa, I. Bombaci, and N. Ortiz, Mon. Not. R. Astron. Soc. **497,** 1488 (2020).

[92] W. Kastaun and F. Galeazzi, Phys. Rev. D **91,** 064027 (2015).

[93] D. Radice, F. Galeazzi, J. Lippuner, L. F. Roberts, C. D. Ott, and L. Rezzolla, Mon. Not. R. Astron. Soc. **460,** 3255 (2016).

[94] V. Nedora, F. Schianchi, S. Bernuzzi, D. Radice, B. Daszuta, A. Endrizzi, A. Perego, A. Prakash, and F. Zappa, Classical Quantum Gravity **39,** 015008 (2022).

[95] K. Hayashi, K. Kawaguchi, K. Kiuchi, K. Kyutoku, and M. Shibata, Phys. Rev. D **103,** 043007 (2021).

[96] S. Chen, L. Wang, K. Hayashi, K. Kawaguchi, K. Kiuchi, and M. Shibata, Phys. Rev. D **110,** 063016 (2024).

[97] F. Foucart, M. D. Duez, L. E. Kidder, H. P. Pfeiffer, and M. A. Scheel, Phys. Rev. D **110,** 024003 (2024).

[98] M. Shibata, K. Kyutoku, T. Yamamoto, and K. Taniguchi, Phys. Rev. D **79,** 044030 (2009).

[99] A. T.-L. Lam et al., arXiv:2410.00137.

[100] N. Stergioulas, A. Bauswein, K. Zagkouris, and H.-T. Janka, Mon. Not. R. Astron. Soc. **418,** 427 (2011).

[101] K. Takami, L. Rezzolla, and L. Baiotti, Phys. Rev. Lett. **113,** 091104 (2014).

[102] K. Takami, L. Rezzolla, and L. Baiotti, Phys. Rev. D **91,** 064001 (2015).

[103] F. Foucart, R. Haas, M. D. Duez, E. O'Connor, C. D. Ott, L. Roberts, L. E. Kidder, J. Lippuner, H. P. Pfeiffer, and M. A. Scheel, Phys. Rev. D **93,** 044019 (2016).

[104] L. R. Weih, M. Hanauske, and L. Rezzolla, Phys. Rev. Lett. **124,** 171103 (2020).

[105] S. Blacker, N.-U. F. Bastian, A. Bauswein, D. B. Blaschke, T. Fischer, M. Oertel, T. Soultanis, and S. Typel, Phys. Rev. D **102,** 123023 (2020).

[106] A. Bauswein, N.-U. F. Bastian, D. B. Blaschke, K. Chatziioannou, J. A. Clark, T. Fischer, and M. Oertel, Phys. Rev. Lett. **122,** 061102 (2019).

[107] A. Bauswein, N.-U. F. Bastian, D. Blaschke, K. Chatziioannou, J. A. Clark, T. Fischer, H.-T. Janka, O. Just, M. Oertel, and N. Stergioulas, AIP Conf. Proc. **2127,** 020013 (2019).